EUROPEAN ORGANIZATION FOR NUCLEAR RESEARCH

Strange particle production in proton-proton collisions at $\sqrt{s} = 0.9$ TeV with ALICE at the LHC

ALICE Collaboration*

This publication is dedicated to the memory of our colleague René Kamermans

Abstract

The production of mesons containing strange quarks (K^0_S, ϕ) and both singly and doubly strange baryons (Λ, $\overline{\Lambda}$, and $\Xi^- + \overline{\Xi}^+$) are measured at central rapidity in pp collisions at $\sqrt{s}$ = 0.9 TeV with the ALICE experiment at the LHC. The results are obtained from the analysis of about 250 k minimum bias events recorded in 2009. Measurements of yields (dN/dy) and transverse momentum spectra at central rapidities for inelastic pp collisions are presented. For mesons, we report yields ($\langle \mathrm{d}N/\mathrm{d}y \rangle$) of 0.184 ± 0.002 (*stat.*) ± 0.006 (*syst.*) for K^0_S and 0.021 ± 0.004 (*stat.*) ± 0.003 (*syst.*) for ϕ. For baryons, we find $\langle \mathrm{d}N/\mathrm{d}y \rangle = 0.048 \pm 0.001$ (*stat.*) ± 0.004 (*syst.*) for Λ, 0.047 ± 0.002 (*stat.*) ± 0.005 (*syst.*) for $\overline{\Lambda}$ and 0.0101 ± 0.0020 (*stat.*) ± 0.0009 (*syst.*) for $\Xi^- + \overline{\Xi}^+$. The results are also compared with predictions for identified particle spectra from QCD-inspired models and provide a baseline for comparisons with both future pp measurements at higher energies and heavy-ion collisions.

*See Appendix A for the list of collaboration members

arXiv:1012.3257v3 [hep-ex] 27 Sep 2017

1   Introduction

The production of hadrons at high transverse momenta in high energy proton-proton collisions is reasonably well described by perturbative Quantum Chromodynamics (pQCD) in terms of hard parton-parton scattering (large momentum transfers) followed by fragmentation [1, 2]. However, the low-momentum region, where most particles are produced and which therefore contributes most to the underlying event, is dominated by soft interactions. In the soft regime, it has been found that particle production can be described effectively by models based on emission from an equilibrated system at a specific temperature and baryo-chemical potential, with additional accounting of conserved quantities [3, 4, 5]. It can also be treated in the framework of QCD inspired phenomenological models, that include multi-parton processes, extrapolated to very low-momentum transfers [6]. The contribution and evolution of multi-parton processes as a function of $\sqrt{s}$ is difficult to establish. Measurements of identified particles at the beam injection energy of the LHC and in the low transverse momentum (p_T) region, along with their comparison with QCD-inspired models, constitute a baseline for comparisons with higher centre-of-mass energies. The low p_T cutoff achievable through the low material budget, low central barrel magnetic field (0.5 T) and excellent particle identification (PID) of the ALICE detectors, allows an accurate measurement of the low momentum region at mid-rapidity.

The differential transverse momentum yields (p_T spectra) and integrated yields at central rapidity of K_S^0, ϕ, Λ, $\overline{\Lambda}$ and $\Xi^- + \overline{\Xi}^+$ have been measured by the ALICE experiment during the commissioning phase of the LHC (December 2009) [7] with the very first proton-proton collisions [8] and are reported in this article. A sample of 250 k minimum bias pp collisions at $\sqrt{s} = 0.9$ TeV has been selected with triggers combining several fast detectors [9]. Measurements are performed using the tracking devices and the main PID detectors of ALICE in the central rapidity region ($|y| < 0.8$). A comparison of the transverse momentum shapes (mass dependence and mean transverse momentum) with PYTHIA [1] and PHOJET [2] is provided.

This article is organized as follows. Section 2 presents the experimental conditions, the minimum bias event selection as well as a brief description of the main detectors and the associated event reconstruction tools used for the analysis. Section 3 is dedicated to the data analysis, including track and topological selections, signal extraction methods and the corresponding efficiency corrections. The determination of the systematic uncertainties are also described in this section. In section 4, the p_T spectra and the integrated yields of the studied particle species are given and compared with previous measurements and model predictions. Conclusions are given in section 5.

2   Experimental set-up and data collection

A detailed description of the ALICE experimental setup and its detector subsystems can be found in [10].

2.1   Main detectors and reconstruction techniques used for the analyses

The central barrel of ALICE covers polar angles from $45°$ to $135°$ over the full azimuth. It is embedded in the large L3 solenoidal magnet providing a nominal magnetic field B of 0.5 T. Within the barrel, the two tracking detectors used in these present analyses consist of an Inner Tracking System (ITS), composed of 6 cylindrical layers of high-resolution Silicon detectors and a cylindrical Time Projection Chamber (TPC). PID is performed using secondary (displaced) vertex reconstruction, invariant mass analysis and single track PID methods, which include the measurement of specific ionization in the ITS and the TPC, and the information from the Time-Of-Flight detector (TOF).

2.1.1   The Inner Tracking System

The Silicon Pixel Detector (SPD) corresponds to the two innermost ITS layers. These two layers have a very high granularity with a total of about 9.8 million pixels, each with a size of 50×425 μm^2. They

are located at radii of 3.9 and 7.6 cm and the pseudorapidity coverages are $|\eta| < 2.0$ and $|\eta| < 1.4$ respectively. The detector provides a position resolution of 12 μm in the rϕ direction and about 100 μm in the direction along the beam axis. It can also deliver a signal for the first level of trigger (L0) in less than 850 ns. The two layers of the Silicon Drift Detector (SDD), located at radii of 15.0 and 23.9 cm, are composed of 260 sensors, including 133 000 collection anodes with a pitch of 294 μm. They provide a charge deposit measurement and a position measurement with a resolution of about 35 μm in the rϕ direction and about 25 μm in the beam direction [11]. The Silicon Strip Detector (SSD) consists of 1698 double-sided sensors (with a strip pitch of 95 μm and a stereo angle of 35 mrad) arranged in 2 layers located at radii of 38 and 43 cm. It provides a measurement of the charge deposited in each of the 2.6 million strips, as well as a position measurement with a resolution of 20 μm in the rϕ direction and about 800 μm in the beam direction.

The ITS sensor modules were aligned using survey information and tracks from cosmic-ray muons and pp collisions. The corresponding methods are described in [11].

The percentage of operational channels in the ITS during the 2009 run is 82% for the SPD, 91% for the SDD and 90% for the SSD.

2.1.2   The Time Projection Chamber

The ALICE TPC is a cylindrical drift detector with a pseudorapidity coverage of $|\eta| \leq 0.9$ [12]. It has a field cage filled with 90 m^3 of Ne/CO$_2$/N$_2$ (85.7/9.5/4.8%). The inner and outer radii of the active volume are of 85 cm and 247 cm respectively and the length along the beam direction is 500 cm. Inside the field cage, ionization electrons produced when charged particles traverse the active volume on either side of the central electrode (a high voltage membrane at -100 kV) migrate to the end plates in less than 94 μs. A total of 72 multi-wire proportional chambers, with cathode pad readout, instrument the two end plates of the TPC which are segmented in 18 sectors and amount to a total of $557,568$ readout pads. The ALICE TPC ReadOut (ALTRO) chip, employing a 10 bit ADC at 10 MHz sampling rate and digital filtering circuits, allows for precise position and linear energy loss measurements with a gas gain of the order of 10^4.

The position resolution in the rϕ direction varies from 1100 μm to 800 μm when going from the inner to the outer radius whereas the resolution along the beam axis ranges between 1250 μm and 1100 μm.

2.1.3   The Time-Of-Flight detector

The ALICE Time-Of-Flight detector [13] is a cylindrical assembly of Multi-gap Resistive Plate Chambers (MRPC) with an inner radius of 370 cm and an outer radius of 399 cm, a pseudorapidity range $|\eta| < 0.9$ and full azimuth angle, except for the region $260 < \phi < 320$ at η near zero where no TOF modules were installed to reduce the material in front of the Photon Spectrometer. The basic unit of the TOF system is a 10-gap double-stack MRPC strip 122 cm long and 13 cm wide, with an active area of 120×7.4 cm^2 subdivided into two rows of 48 pads of 3.5×2.5 cm^2. Five modules of three different types are needed to cover the full cylinder along the z direction. All modules have the same structure and width (128 cm) but differ in length. The overall TOF barrel length is 741 cm (active region). It has 152,928 readout channels and an average thickness of $25 - 30\%$ of a radiation length, depending on the detector zone. For pp collisions, such a segmentation leads to an occupancy smaller than 0.02 %. Its front-end electronics is designed to comply with the basic characteristics of a MRPC detector, i.e. very fast differential signals from the anode and cathode readout. Test beam results demonstrated a time resolution below 50 ps, dominated by the jitter in the electronic readout.

2.1.4 The VZERO Counters

The VZERO counters are two scintillator hodoscopes located along the beam direction at -0.9 m and 3.3 m from the geometrical centre of the experiment. They correspond to a coverage of $-3.7 < \eta < -1.7$ and $2.8 < \eta < 5.1$ respectively and have a time resolution close to 0.5 ns. They are used as trigger detectors and help to remove beam-gas interaction background.

2.1.5 Track reconstruction and particle identification

The global tracking system in the ALICE central barrel (combining the ITS and the TPC) covers the pseudorapidity window $|\eta| < 0.9$.

The reconstruction in the tracking detectors begins with charge cluster finding. The two coordinates of the crossing points (space points) between tracks and detector sensitive elements (pad rows in the TPC, and silicon sensors in the ITS) are calculated as the centres of gravity of the clusters. The errors on the space point positions are parametrized as functions of the cluster size and of the deposited charge. In the TPC, these errors are further corrected during the tracking, using the crossing angles between tracks and the pad rows.

The space points reconstructed at the two innermost ITS layers (pixel detector, SPD) are then used for the reconstruction of the primary vertex. One space point from the first SPD layer and one from the second layer are combined into pairs called "tracklets". The primary vertex is consequently reconstructed in 3D as the location that minimizes the sum of the squared distances to all the tracklet extrapolations. If this fails, the algorithm instead reconstructs the z coordinate of the vertex by correlating the z coordinates of the SPD space points, while for x and y the average position of the beam in the transverse plane (measured basis by a dedicated calibration procedure on a run-by-run basis) is assumed.

Track reconstruction in ALICE is based on the Kalman filter approach and is discussed in detail in [15]. The initial approximations for the track parameters (the "seeds") are constructed using pairs of space points taken at two outer TPC pad rows separated by a few pad rows and the primary vertex. The primary vertex position errors for this procedure are considered to be as big as 3 cm. The seeds for the secondary tracks are created without using the primary vertex, since such a constraint would unnecessarily reduce the V0 finding efficiency. The space points are searched along the line connecting the pairs of points taken at those two outer TPC pad rows.

Once the track seeds are created, they are sorted according to the estimate of their transverse momentum (p_T). Then they are extended from one pad row to another in the TPC and from one layer to another in the ITS towards the primary vertex. Every time a space point is found within a prolongation path defined by the current estimate of the covariance matrix, the track parameters and the covariance matrix are updated using the Kalman filter. For each tracking step, the estimates of the track parameters and the covariance matrix are also corrected for the mean energy loss and Coulomb multiple scattering in the traversed material. The decision on the particle mass to be used for these corrections is based on the dE/dx information given by the TPC when available. If the information is missing or not conclusive, a pion mass is assumed. Only five particle hypotheses are considered: electrons, muons, pions, kaons and protons.

All the tracks are then propagated outwards, through the ITS and the TPC. When possible, they are matched with the hits reconstructed in the TOF detector. During this tracking phase, the track length and five time-of-flight hypotheses per track (corresponding to the electron, muon, pion, kaon and proton masses) are calculated. This information is later used for the TOF PID procedure. The track parameters are then re-estimated at the distance of closest approach (DCA) to the primary vertex applying the Kalman filter to the space points already attached. Finally, the primary vertex is fitted once again, now using reconstructed tracks and the information about the average position and spread of the beam-beam interaction region estimated for this run.

In pp collisions, the track reconstruction efficiency in the acceptance of TPC saturates at about 90% because of the effect of the dead zones between its sectors. It goes down to about 75% around $p_T = 1$ GeV/c and drops to 45% at 0.15 GeV/c. It is limited by particle decays (for kaons), track bending at low p_T and absorption in the detector material. The amount of material traversed by particles near $\eta = 0$ is about 11% of of a radiation length including the beam pipe, the ITS and the TPC (with service and support).

The overall p_T resolution is at least as good as the TPC-standalone resolution, which is typically 1% for momenta of 1 GeV/c and 7% for momenta of 10 GeV/c, and follows the parameterization $(\sigma(p_T)/p_T)^2 = (0.01)^2 + (0.007\ p_T)^2$ where p_T is expressed in GeV/c (see [14] for the details).

The resolution of the track transverse impact parameter (the minimal distance between a track and the primary vertex in the transverse plane) depends on the precision of track and primary vertex reconstruction. These in turn depend on the momentum, and, in the case of the vertex, on the number of contributing tracks. As it was estimated from the data, the transverse impact parameter resolution for a typical pp event could be parameterized as $\sigma(p_T) = 50 + 60/(p_T)^{0.9}$ (σ is in μm, and p_T is in GeV/c), which was defined by the level of the ITS alignment achieved in 2009.

The dE/dx resolution of the TPC is estimated to be about 5% for tracks with 159 clusters [12], which is better than the design value [15]. When averaged over all reconstructed tracks, this resolution is about 6.5%.

During the run, the preliminary calibration of the TOF detector corresponds to a resolution of 180 ps, which includes 140 ps due to the jitter in the absolute time of the collisions. This contribution is reduced to about 85 ps for those events with at least 3 tracks reaching the TOF, in which case an independent time zero determination is possible. The matching efficiency with TPC tracks (which includes geometry, decays and interaction with material) is on average 60% for protons and pions and reaches 65% above $p_T = 1$ GeV/c. For kaons it remains sligthly lower [16]. Above $p_T = 0.5$ GeV/c, the TOF PID has an efficiency larger than 60% with a very small contamination.

2.2 LHC running conditions and triggers

For the first collisions provided by the Large Hadron Collider, four low intensity proton bunches (10^9 protons per bunch, giving the luminosity of the order of 10^{26} cm^{-2}s^{-1}) per beam were circulated, and two pairs of them crossed at the ALICE interaction point. Under such conditions, the rate for multiple events in a given bunch-crossing ("pile-up") was negligible. The energy in the centre of mass corresponded to twice the beam injection energy, that is $\sqrt{s} = 0.9$ TeV. The data acquisition of ALICE was triggered by requiring two coincidence conditions: i) the LHC bunch-crossing signal together with the two beam pick-up monitors (BPTX); ii) ALICE minimum bias (MB) trigger requiring a combination of signals from the SPD and from the VZERO counters. For these analyses, the MB$_{OR}$ was used, which is fulfilled when at least one of the VZEROs or the SPD trigger is fired [9]. The corresponding data rate was ~ 10 Hz.

3 Data analysis

3.1 Event and track selection

The primary vertex is reconstructed using either SPD tracklets [8] (5% of the events) or global tracks (95% of the events). Events are selected by requiring that the distance between the position of primary vertex and the geometrical centre of the apparatus along the beam axis be less than 10 cm ($\bar{z} = -0.40$ cm and rms$_z = 4.24$ cm, where $\bar{z}$ is the average position of the primary vertex along the beam axis). Events with less centred primary vertices ($|z| > 10$ cm) are discarded in order to minimize acceptance and efficiency biases for tracks at the edge of the TPC detection volume. The average position and dispersion for both horizontal and vertical directions are found to be $\bar{x} = -0.35$ mm ($\bar{y} = +1.63$ mm) and rms$_x =$
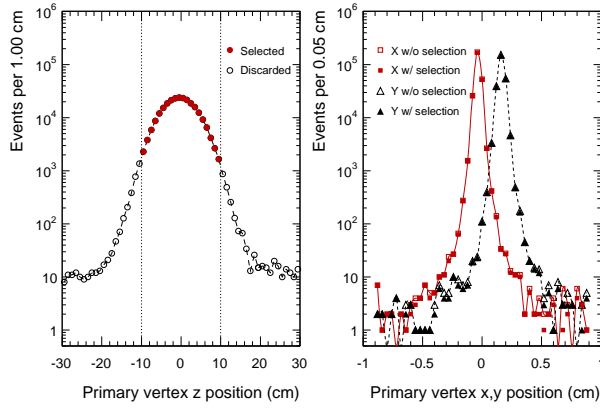
Fig. 1: Primary vertex distributions for the analysed events. The left panel shows the distributions along the beam axis. Selected events (full symbols) are required to have a reconstructed primary vertex with $|z| < 10$ cm. The right panel corresponds to the directions perpendicular to the beam axis: horizontally (i.e. x-direction, squares and full line) and vertically (i.e. y-direction, triangles and dashed line).

0.23 mm ($\text{rms}_y = 0.27$ mm). No conditions were applied on the x and y position of the vertex. The total number of events used for obtaining the particle spectra and yields is about 250 k events. Figure 1 shows the primary vertex distribution along the beam axis (left panel) and for the x and y directions (right panel). The dashed lines indicate the limits of the selected vertex region.

The normalization to the number of inelastic events (INEL) is obtained in the same way as other ALICE analyses [8, 16]. It leads to a correction for the normalization of $\sim 5\%$ with an uncertainty of 2%. This uncertainty is added to the ones described in section 3.5 and mainly related to the modeling of the fraction of diffractive events with several Monte Carlo event generators.

Several quality criteria are defined for track selection. Each track is required to have been reconstructed in the TPC in the initial outward-in step of tracking and then successfully refitted in the final back-propagation to the primary vertex as described in section 2.1.5. It is also required that each track has at least 80 TPC clusters out of a maximum of 159. At the reconstruction level, split tracks are rejected as well as those which may correspond to daughters of kaons decaying in the TPC.

As the ϕ particle is a strongly decaying resonance, its daughters are indistinguishable from primary particles at the reconstruction level and therefore primary track selections are used. As a first step, each track is propagated to the reconstructed primary vertex. If this operation is successful, the track is kept if it has a DCA smaller than 5 mm (3 cm) in the transverse (longitudinal) direction with the additional constraints of having at least one SPD cluster and a χ^2 of less than 4 per cluster assignment (for each cluster, the χ^2 has two degrees of freedom).

Depending on its lifetime, a particle may cross several layers of the ITS before weakly decaying. The probability that the daughter tracks of K_S^0, Λ, $\overline{\Lambda}$ and $\Xi^- + \overline{\Xi}^+$ have a hit in this detector decreases accordingly. Therefore, no specific condition on the number of ITS hits is required for the daughter tracks of the reconstructed secondary vertices. However, other quality criteria are applied for selecting the daughter tracks of weakly decaying particles which are not considered as primaries. The selections described are summarized in Table 1. The measurement of differential yields in rapidity and p_T bins cannot be performed simultaneously for the particles considered due to the small available statistics. Therefore the rapidity ranges are chosen such that i) the efficiency does not vary strongly for each species and ii) the rapidity distribution is sufficiently flat for it to be possible to rely on the Monte Carlo to obtain the corrections.

6

Table 1: Track selection criteria.

Common selections		
Detectors required for track rec./fit		ITS,TPC
Number of TPC clusters [a]	$>$	80
N(σ) dE/dx (TPC PID)		3 to 5
Primary track selections		
χ^2 per cluster	$<$	4
DCA to primary vertex (r,z)	$<$	$(0.5, 3.0)$ cm
Number of SPD clusters [b]	$\geq$	1
Secondary track selections		
transverse momentum [c]	$>$	160 MeV/c

[a] maximum number for the TPC is 159;
[b] maximum number for the SPD is 2;
[c] in the cases of K_S^0, Λ and $\overline{\Lambda}$.

Table 2: Secondary vertex selection criteria.

Common selections		
Minimum transverse decay radius	$>$	0.2 cm
Maximum transverse decay radius	$<$	100 cm
$V0$ vertex selections (K_S^0, Λ and $\overline{\Lambda}$)		
DCA of V0 daugther track to primary vertex	$>$	0.05 cm
DCA between V0 daughter tracks	$<$	0.50 cm
Cosine of V0 pointing angle (Λ and $\overline{\Lambda}$)	$>$	0.99
Cascade vertex selections		
DCA of cascade daughter track to primary vertex [a]	$>$	0.01 cm
DCA between V0 daughter tracks	$<$	3.0 cm
Cosine of V0 pointing angle	$>$	0.97
DCA of V0 to primary vertex	$>$	0.001 cm
V0 invariant mass	$>$	1110 MeV/c^2
V0 invariant mass	$<$	1122 MeV/c^2
DCA between V0 and bachelor track	$<$	3.0 cm
Cosine of cascade pointing angle	$>$	0.85

[a] for bachelor and each V0 daughter.

Table 3: Main characteristics of the reconstructed particles: valence quark content, mass, $c\tau$ and charged decay branching ratio (B.R.) [18].

	Particles	mass (MeV/c^2)	$c\tau$	charged decay	B.R. (%)
Mesons	K_S^0	497.61	2.68 cm	$K_S^0 \rightarrow \pi^+ + \pi^-$	69.2
	ϕ ($s\bar{s}$)	1019.46	45 fm	$\phi \rightarrow K^+ + K^-$	49.2
Baryons	Λ (uds) and $\overline{\Lambda}$ ($\overline{uds}$)	1115.68	7.89 cm	$\Lambda \rightarrow p + \pi^-$ and $\overline{\Lambda} \rightarrow \overline{p} + \pi^+$	63.9
	Ξ^- (dss) and $\overline{\Xi}^+$ ($\overline{dss}$)	1321.71	4.91 cm	$\Xi^- \rightarrow \Lambda + \pi^-$ and $\overline{\Xi}^+ \rightarrow \overline{\Lambda} + \pi^+$	99.9

3.2 Particle reconstruction and identification methods

3.2.1 *Topological reconstruction of* K_S^0*,* Λ*,* $\overline{\Lambda}$ *and* $\Xi^- + \overline{\Xi}^+$

The K_S^0, Λ, $\overline{\Lambda}$ and $\Xi^- + \overline{\Xi}^+$ are identified by applying selections on the characteristics of their daughter tracks (see Table 2) and using their weak decay topologies in the channels listed in Table 3.

The measurement of K_S^0, Λ and $\overline{\Lambda}$ is based on the reconstruction of the secondary vertex (V0) associated to their weak decay. The V0 finding procedure starts with the selection of secondary tracks, i.e. tracks having a sufficiently large impact parameter with respect to the primary vertex. All possible combinations between two secondary tracks of opposite charge are then examined. They are accepted as V0 candidates only if the DCA between them is smaller than 0.5 cm. The minimization of the distance between the tracks is performed numerically using helix parametrizations in 3D. The V0 vertex position is a point on the line connecting the points of closest approach between the two tracks. Its distance from each daughter track is taken to be proportional to the precision of the track parameter estimations. Once their position is determined, only the V0 candidates located inside a given fiducial volume are kept. The inner boundary of this fiducial volume is at a radius of 0.2 cm from the primary vertex, while the outer limit is set at 100 cm. Finally, for Λ and $\overline{\Lambda}$ reconstruction, the V0 finding procedure checks whether the particle momentum ($\vec{p}$) associated with the V0 candidate (calculated as the sum of the track momenta extrapolated to the position of the DCA) points back to the primary vertex. This is achieved by applying a cut on the cosine of the angle (pointing angle $\theta_{\vec{p}}$) between $\vec{p}$ and a vector connecting the primary vertex and the V0 position ($\cos\theta_{\vec{p}} > 0.99$). The invariant mass of each candidate can then be calculated either under the K_S^0 or the Λ hypothesis.

The TPC PID helps substantially to remove the combinatorial background for the Λ and $\overline{\Lambda}$ (mainly for the baryon daughter identification, while it is not needed for the K_S^0 decaying into pions). TPC PID is described in paragraph 3.2.3. The selections here concern the proton daughter only and have been chosen to be looser for the daughter track with momentum below 0.7 GeV/c ($\pm 5\sigma$) and tighter for higher momentum ($\pm 3\sigma$).

The $\Xi^- + \overline{\Xi}^+$ particles are identified via their "cascade" decay topology. The cascade finding procedure starts from the V0 finding procedure for the Λ daughter but with less stringent selection criteria (see Table 2 and Cascade vertex selections). This is done to increase the efficiency and to allow for the fact that the daughter Λ's do not have to point back to the primary vertex.

The V0 candidates found within the Λ mass window (1116 ± 6 MeV/c^2) are combined with all possible secondary tracks (bachelor candidates) with the exception of both V0 daughter tracks. A cut on the impact parameter of the bachelor track is applied to reject the primary particles which increase the combinatorial background.

A V0-bachelor association is performed if the distance of closest approach between the bachelor track and the V0 trajectory (DCA between V0 and bachelor track) is small (less than 3 cm). Finally, this
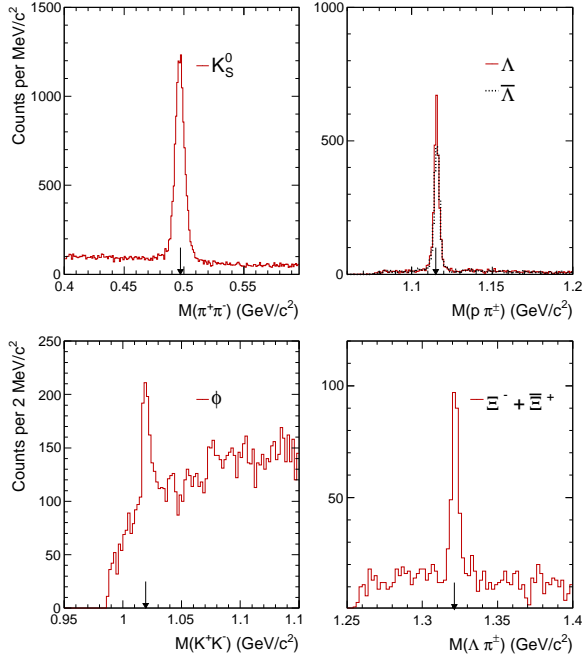
Fig. 2: Invariant mass distributions of K_S^0, Λ and $\overline{\Lambda}$, ϕ and the sum $\Xi^- + \overline{\Xi}^+$. The vertical arrows indicate the nominal mass values from PDG.

cascade candidate is selected if its reconstructed momentum points back to the primary vertex (cosine of cascade pointing angle). The cascade finding is limited to the fiducial region used for V0 reconstruction (see Table 2).

In addition to topological selections, the reconstruction of cascades also makes use of the single-track PID information delivered by the TPC. This is considered for each of the three daughters (both pions and the proton). For each track, a loose selection is required ($\pm 4\sigma$ over the whole momentum range) to reject the combinatorial background in part. The resulting invariant mass distributions are presented in Fig. 2.

3.2.2 Additional quality checks for K_S^0, Λ, $\overline{\Lambda}$

A significant fraction of the reconstructed V0 come from γ conversion in the detector material. This can be clearly seen in the Armenteros-Podolanski distribution [17] shown in Fig. 3 where p_L^+ and p_L^- are the longitudinal components of the total momentum for the positive and negative daughters respectively, relative to the direction of the V0 momentum vector. The K_S^0, Λ and $\overline{\Lambda}$ signal regions are symmetric and clearly distinguishable.

The lifetime ($c\tau$) distributions for K_S^0, Λ and $\overline{\Lambda}$ are also checked. All V0 candidates within a $\pm 3\sigma$ effective mass region around the nominal value are used in the distribution without further residual background subtraction. The corresponding distributions of $c\tau = L\frac{m}{p}$ are obtained, where L is defined as the distance between primary and V0 vertices, and m and p are the particle mass and momentum. Because of the acceptance, the single track efficiency and the topological selections applied at reconstruction level, the reconstruction efficiency as a function of the decay length is not constant. The corresponding corrections are extracted from the reconstruction of full Monte Carlo simulations (see section 3.4). The corrected $c\tau$ distributions are fitted using exponential functions. The results are shown with the statistical uncertainties in Fig. 4. The extracted decay lengths of 7.9 ± 0.1 cm, 7.7 ± 0.1 cm and 2.72 ± 0.03 cm for Λ, $\overline{\Lambda}$ and K_S^0, respectively, are compatible with the PDG values given in Table 3.

9
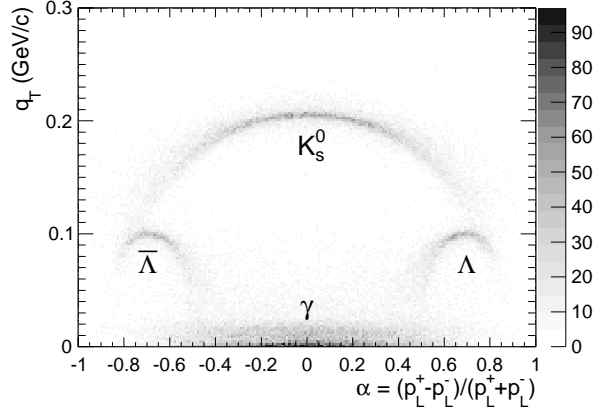
Fig. 3: Armenteros-Podolanski distribution for V0 candidates showing a clear separation between K^0_S, Λ and $\overline{\Lambda}$. The γ converting to e^+e^- with the detector material are located in the low q_T region, where q_T is the momentum component perpendicular to the parent momentum vector.
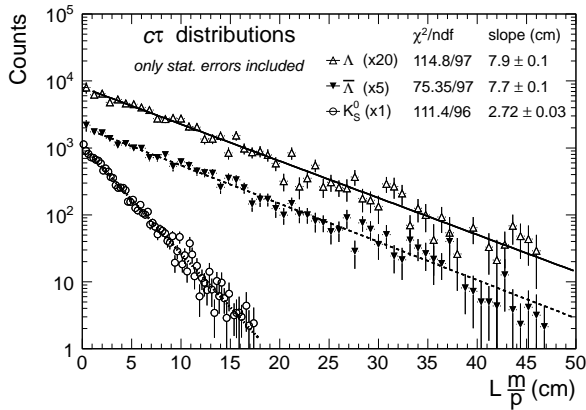
Fig. 4: K^0_S, Λ and $\overline{\Lambda}$ lifetime distributions obtained for the candidates selected by the invariant mass within a $\pm 3\sigma$ region around the nominal mass and corrected for detection efficiency. The distributions are scaled for visibility and fitted to an exponential distribution (straight lines). Only statistical uncertainties are shown.
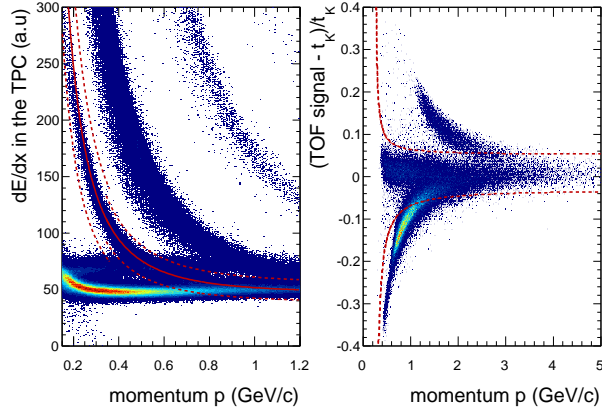
Fig. 5: Left panel shows the distribution of the measured energy-deposit of charged particles versus their momentum in the TPC. The dashed lines delimit successively a $\pm 5\sigma$ then a $\pm 3\sigma$ selection of the kaon tracks using the ALEPH parameterization [19] of the Bethe-Bloch curve (solid line). Right panel shows the relative difference between TOF measured times and that corresponding to a kaon mass hypothesis. The dashed lines delimit a coarse fiducial region compatible with this kaon hypothesis.

3.2.3 ϕ reconstruction

The ϕ resonance is reconstructed through its principal decay channel $\phi \to K^+K^-$ (see Table 3). With a $c\tau$ of 45 fm, its decay vertex is indistinguishable from the primary collision vertex. Therefore the selection criteria adopted for the candidate daughter tracks are the ones used for primaries, as specified in Table 1.

A crucial issue for the ϕ reconstruction, as for any strongly decaying resonance, is the combinatorial background determination. In the present analysis PID is used to select kaons, rejecting most of the background while leading to a very small loss in efficiency. For this purpose, tracks are selected if the PID information from the TPC is compatible with a kaon signal and using the TOF signal when available.

For each track, the expected energy loss is calculated using a parametrised response based on the Bethe-Bloch formula [19] computed with a kaon mass hypothesis. It is compared with the TPC specific ionization dE/dx measured via truncated mean (the reconstructed momentum being evaluated at the inner radius of the TPC). With the current TPC calibration for this data set, the assumed dE/dx resolution is 6 %. For momenta smaller than 350 MeV/c, the species are well separated so the window is set to $\pm 5\sigma$ with little or no contamination; above 350 MeV/c, it is set instead to $\pm 3\sigma$ as shown in the left panel of Fig. 5.

The accepted band for TOF kaon identification is defined with two hyperbolas as shown in the right panel of Fig. 5.

3.3 Background evaluation and signal extraction

For minimum bias pp collisions, the signals for all particles are clearly distinguishable from the combinatorial background as shown in Fig. 2. Two different methods are used to extract the invariant mass signal from the background. For the single strange particles (K^0_S, Λ and $\overline{\Lambda}$), the signal is first approximated by a Gaussian on a second order polynomial background. This gives an estimate of the signal mean and width although the invariant mass signal is not strictly Gaussian. Then the background is sampled on each side of the signal by using both sampled regions that are more than 6σ away from the Gaussian mean. The assumption that no reconstructed signal is included in these regions is checked using Monte Carlo data. The width of the background regions can vary depending on the p_T interval considered in the invariant mass distributions. The sum of signal and background ($S+B$) is sampled in the region defined by the mean $\pm 4\sigma$.
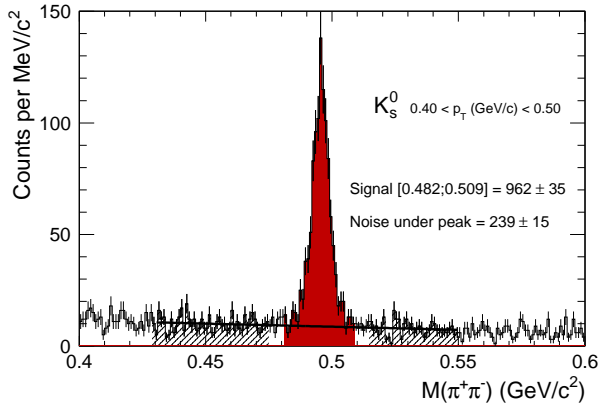
Fig. 6: Plot illustrating the "bin-counting" method used to extract the raw yields. It corresponds to the invariant mass distribution of K_S^0 for the p_T bin $[0.4 - 0.5]$ GeV/c. The hashed regions show where the background is sampled; they are chosen to be 6σ away from the signal approximated with a Gaussian distribution. The averaged or fitted background is subtracted from the signal region of $\pm 4\sigma$.

The sampling method is illustrated in Fig. 6 for the K_S^0. Two methods are used to evaluate the background and give consistent results. The background areas are either i) fitted simultaneously with polynomial functions (from first to third order) or ii) averaged by simply counting the number of entries ("bin-counting"). The background B under the signal S is estimated using the normalized area sampled on both sides of the signal region (Gaussian mean $\pm 4\sigma$). The signal yield $S = (B + S) - B$ is thus evaluated without any assumption as to its shape. Systematic effects such as signal asymmetry are taken into account by varying the size of the signal and background intervals up to 1σ. The difference between the two methods (fit and bin-counting) contributes to the evaluation of the systematic uncertainties associated to the signal extraction.

In the case of the $\Xi^- + \overline{\Xi}^+$, statistical uncertainties are significant so that, in parallel to the bin-counting method, the background level is simply estimated by a straight line fit.

The ϕ invariant mass distribution has a larger combinatorial background and a function reproducing both the background and the signal is preferred. It is found that the background can be well reproduced by a function $f(M) = a\sqrt{M - b}$, while the peak has the shape of a Gaussian. The peak range is defined as $\pm 4\sigma$ around the PDG mass of the ϕ, where $\sigma = \Gamma/2.35$ and Γ is the nominal value of the resonance full width at half maximum (4.5 MeV/c^2) [18]. For each analyzed p_T bin, several fit ranges are investigated. It is found that the fitted width matches that extracted from a full Monte Carlo simulation (as defined in section 3.4) within 5%, except for the last p_T bin where it is broader ($\sim 10\%$). While fluctuations of the fit values as a function of the fit range are taken into account for the systematic error (see section 3.5.1), the fit values used for all subsequent steps in the analysis are those that minimize the difference $|\chi^2/\text{NDF} - 1|$. Figure 7 illustrates the method for the $[1.0 - 1.5]$ GeV/c p_T bin. Every unlike-sign track pair passing all selection criteria and falling within the ϕ invariant mass peak range is counted. The total number of ϕ is estimated by subtracting the integral of the background function alone, computed in the same invariant mass range.

The signal counts (raw yields) for each of the p_T bins are histogrammed as a function of p_T for K_S^0, Λ, $\overline{\Lambda}$ in Fig. 8 and for ϕ and $\Xi^- + \overline{\Xi}^+$ in Fig. 9. The uncertainties correspond to both the statistical errors related to the number of counts and the systematics from the bin-counting and fit methods used to extract the signal from the background.
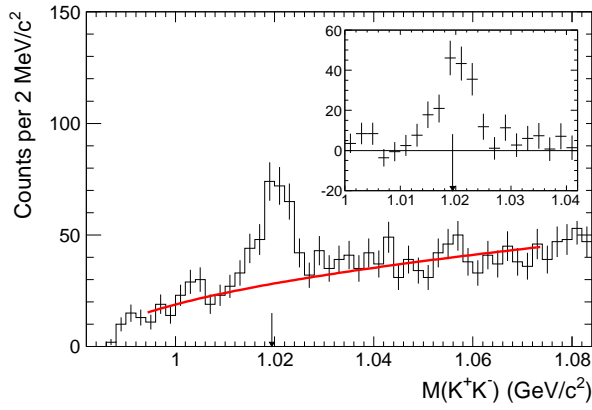
Fig. 7: Background evaluation for the ϕ corresponding to the p_T bin [1.0-1.5] GeV/c. The inset shows the ϕ signal after background subtraction. The vertical arrows indicate the nominal mass value from PDG.
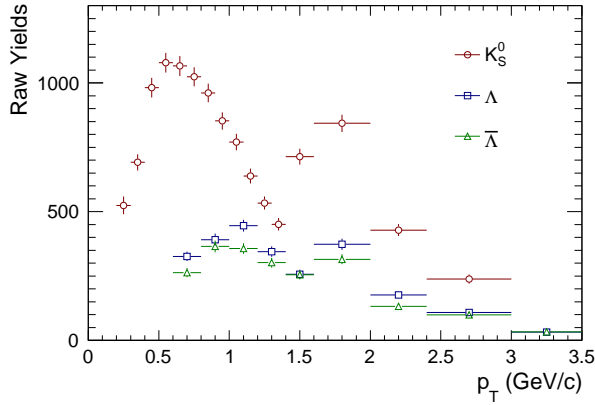

Fig. 8: Reconstructed (raw) yields of K^0_S (open circles), Λ (open squares) and $\overline{\Lambda}$ (open triangles) as a function of p_T. The change of bin size results in successive offsets of the raw counts at $p_T = [1.4, 1.6, 2.4]$ GeV/c for K^0_S and $p_T = [1.6, 2.4, 3.0]$ GeV/c for Λ and $\overline{\Lambda}$. Uncertainties correspond to the statistics and the systematics from the signal extraction. They are represented by the vertical error bars. The horizontal error bars give the bin width.
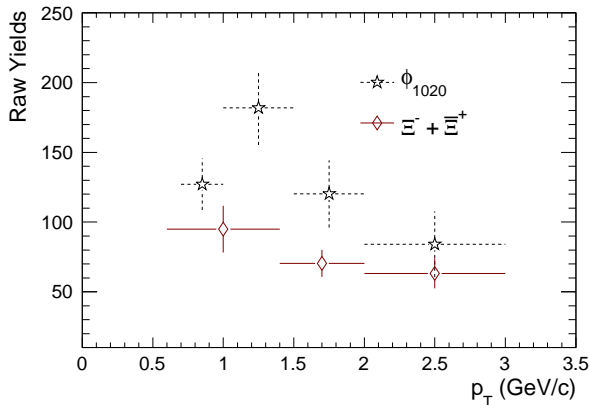
Fig. 9: Reconstructed (raw) yields of ϕ (stars) and $\Xi^- + \overline{\Xi}^+$ (diamonds) as a function of p_T. With the current statistics, 4 p_T bins are used for the ϕ ([0.7-1.0], [0.7-1.5], [1.5-2.0] and [2.0-3.0] GeV/c) and 3 p_T bins for the $\Xi^- + \overline{\Xi}^+$ ([0.6-1.4], [1.4-2.0] and [2.0-3.0] GeV/c). Uncertainties correspond to the statistics (i.e. the number of reconstructed particles) and the systematics from the signal extraction. They are represented by the vertical error bars (the horizontal ones give the bin width).

13
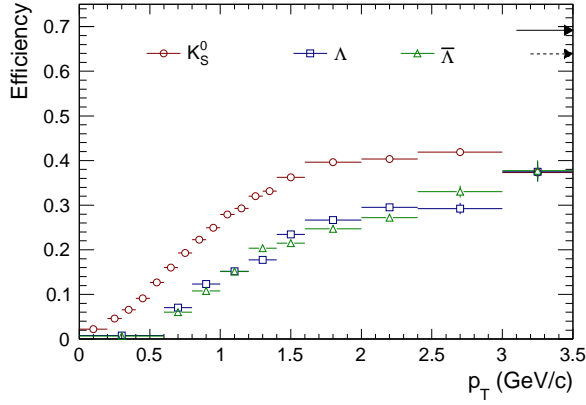
Fig. 10: Efficiency of K_S^0 (open circles), Λ (open squares) and $\overline{\Lambda}$ (open triangles) as a function of p_T. The uncertainties correspond to the statistics in Monte Carlo samples used to compute the corrections. The efficiency is limited by the branching ratio represented by a solid arrow for K_S^0 (0.692) and by a dashed arrow for Λ and $\overline{\Lambda}$ (0.639).
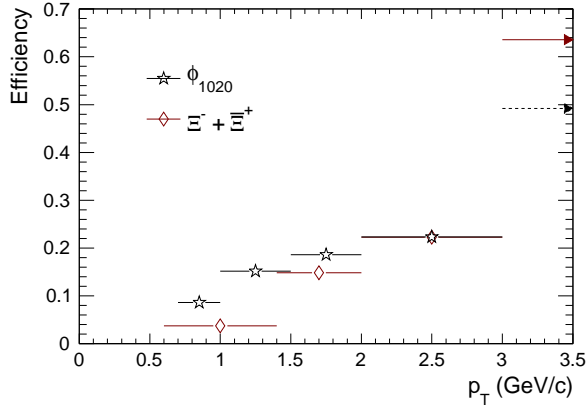
Fig. 11: Efficiency of ϕ (stars) and $\Xi^- + \overline{\Xi}^+$ (diamonds) as a function of p_T. The uncertainties correspond to the statistics in the Monte Carlo sample used to compute the corrections. The efficiency is limited by the branching ratio represented by a solid arrow for $\Xi^- + \overline{\Xi}^+$ (0.636) and by a dashed arrow for ϕ (0.492).

3.4 Efficiency corrections

The efficiency corrections are obtained by analysing Monte Carlo (MC) events in exactly the same way as for the real events. Little dependence is found on the several MC generators which are used. Therefore the corrections presented here are obtained using the event generator PYTHIA 6.4 (tune D6T) [1, 20] and GEANT3 [21] for particle transport through the ALICE detectors.

The MC information is propagated through the whole reconstruction and identification procedure to generate the differential p_T efficiencies as shown in Fig. 10 for K_S^0, Λ and $\overline{\Lambda}$ and in Fig. 11 for ϕ and $\Xi^- + \overline{\Xi}^+$. The uncertainties correspond to the statistics of Monte Carlo samples used to compute the corrections. For all particles, the global efficiency is limited at low p_T because of the acceptance of at least two charged daughter tracks in the detection volume of the TPC (three tracks in the case of $\Xi^- + \overline{\Xi}^+$). It rapidly increases with p_T but cannot exceed the asymptotic limits given by the charged particle decay branching ratios presented in Table 3. The difference between the Λ and $\overline{\Lambda}$ reflects the absorption of the anti-proton daughter of the $\overline{\Lambda}$. For all the variables used to select the particles and improve the signal over noise ratio (see Tables 1 and 2), it is verified that data and MC distributions match, thus possible efficiency biases can be properly managed. Examples of such distributions are presented in Fig. 12.

14
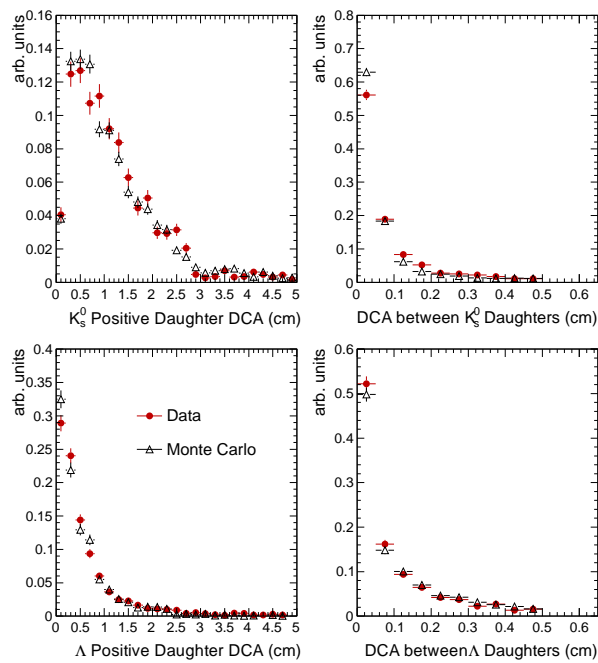
Fig. 12: Comparison between data (red circles) and Monte Carlo (black open triangles) for several topological variables used to select secondary vertices. The top panels correspond to the K_S^0 candidates selected in a ± 20 MeV/c^2 invariant mass window around the nominal mass. The distribution of the DCA between the positive daughter track and the primary vertex and the DCA distribution between the two daughters tracks are displayed in the left and the right top panels respectively. On the bottom panels, the same distributions are shown for the Λ candidates selected in a ± 8 MeV/c^2 invariant mass window around the nominal mass.

Table 4: Point-to-point systematic uncertainties expressed in percentage for p_T spectra of different particles. For each particle, the reported values correspond to the effect on the lowest p_T bin, the average and the highest p_T bin, except for the feed-down contributions where values are estimated as being constant versus p_T or where the effect is found to be negligible (less than 2 standard deviations from the default value on the corrected spectrum).

systematic effects (%)	K^0_S	Λ	$\overline{\Lambda}$	ϕ	$\Xi^- + \overline{\Xi}^+$
Selections					
tracks	$[4.6 - 1.1 - 2.1]$	$[2.6 - 2.0 - 2.5]$	$[3.0 - 2.0 - 4.1]$	$[0.9 - 3.1 - 6.0]$	$[negl. - 5.4 - negl.]$
topological	$[3.8 - 1.4 - 1.3]$	$[3.3 - 3.3 - 1.5]$	$[4.7 - 4.7 - 3.8]$	$--$	$[6.8 - 11.6 - 13.9]$
Signal extraction	$[4.5 - 1.5 - 1.5]$	$[3.0 - 2.0 - 5.0]$	$[3.0 - 2.0 - 5.0]$	$[3.2 - 4.3 - 7.0]$	$[5.6 - negl. - 2.5]$
TPC dE/dx	$--$	$[5 - negl.]$	$[5 - negl.]$	$[1.8 - 2.9 - 3.6]$	$[negl.]$
Efficiency					
material budget	$[1.5 - 1.5 - 1.1]$	$[3.4 - 1.0 - 1.6]$	$[3.7 - 2.0 - 4.5]$	$[4.7 - 4.0 - 2.3]$	$[2.7 - 1.5 - 3.6]$
$\bar{p}$ cross-section	$--$	< 1	< 2	$--$	< 2
Feed-down	$--$	1.7	1	$--$	$--$

3.5   Estimation of the systematic uncertainties

Systematic uncertainties are discussed in the following sections, where details are given on the contributions due to topological selections and signal extraction methods, as well as those due to material budget and feed-down. As for efficiency corrections, MC data are generated with PYTHIA 6.4 (tune D6T) [1, 20] and transported with GEANT3 [21]. At low p_T, the anti-proton absorption cross section in GEANT3 is known to be too large [22, 23]. GEANT4 (with the absorption cross-sections of [24]) was then used to correct the anti-proton tracking efficiency. The information is summarized in Table 4. In addition to these point-to-point systematic uncertainties, there is also a 2 % systematic error on the global normalization coming from the evaluation of the total number of inelastic events.

3.5.1   Systematic uncertainties due to track or topological selections and signal extraction

Systematic uncertainties due to tracking and topological identification are determined by varying the track and topological (for secondary vertices) selections, as well as the definition of the regions sampled for signal extraction. To assess the different systematic uncertainties, only the deviations that are statistically significant are taken into account (more than 2 standard deviations away from the central value on the corrected spectrum).

The systematic variation of track and topological selections results in a variation of the amount of signal extracted from invariant mass distribution in both data and the Monte Carlo simulation mentioned above. The difference between these amounts of signal corresponds indirectly to the accuracy with which the MC simulation reproduces the characteristics of real events, from the simulation of the detector response to the background shape and composition considered for the extracted signal. It is estimated that the point-to-point uncertainties in the p_T spectra are at most 4.6 %, 3.3 %, 4.7 %, 6 % and 13.9 % for the K^0_S, Λ, $\overline{\Lambda}$, ϕ and $\Xi^- + \overline{\Xi}^+$, respectively. The systematic uncertainties of the signal extraction for K^0_S, Λ, $\overline{\Lambda}$ and $\Xi^- + \overline{\Xi}^+$ are p_T-dependent and estimated by varying the invariant mass regions where the signal and the background are sampled using the bin-counting method described in section 3.3. For the ϕ signal, the systematic uncertainties from background subtraction are estimated using three different criteria. First of all, the function reproducing the background is replaced by a second or third order polynomial. Moreover, the fit is repeated fixing the width parameter to $\pm 10\%$ of the value obtained in the default procedure (described in section 3.3), and also to the value obtained when fitting the Monte Carlo sample and to $\pm 10\%$ of this. Finally, the fit range is also varied. All of these computations result in a variation of the raw counts with respect to those shown in Fig. 9. Although a quite large compatibility region is

requested for PID (at least 3σ) the effects of varying the dE/dx selections are taken into account for the corresponding efficiency calculation. For both ϕ and $\Xi^- + \overline{\Xi}^+$, statistical errors dominate after signal extraction (see section 3.3) and consequently, some systematic effects due to PID are extrapolated from single track and V0 measurements. The TOF PID selection is applied only to reject the ϕ background. No systematic effects are observed on the ϕ signal i) for the Monte Carlo data sample, when the selection is applied to the ϕ daughters in addition to all other cuts; ii) for real events, when comparing the ϕ statistics before and after applying the selection.

3.5.2 *Systematic uncertainties due to material budget and absorption cross-section*

A dedicated study involved the variation of the detector material thickness crossed by particles. The material budget uncertainty, based on γ conversion measurements, is estimated to be 7% in terms or radiation length [22]. The efficiency variation due to this material budget uncertainty depends on the momentum of each of the decay daughters. Although such a variation is also correlated with the momentum of the parent particle, the corresponding systematic uncertainties are reported as point-to-point errors in Table 4 for the lowest, the average and the highest p_T bin and eventually added in quadrature to the total systematic errors.

Specific uncertainties are related to the (anti-)proton absorption and scattering cross-sections used for propagating these particles through the geometry of the detectors with both GEANT3 [21] (and its default absorption cross-sections) and GEANT4 (using the absorption cross-sections of [24]). More details about the modifications can be found in [22, 23] and references therein. The corresponding corrections are taken into account in the efficiency versus p_T assuming that absorption cross-sections are identical for the (anti-) hyperon and its (anti-) proton daughter. The uncertainties associated with these corrections are derived from the (anti-)proton cross-section uncertainties and the values are estimated as constant and lower than 1% (2%) for Λ ($\overline{\Lambda}$) and 2% for $\Xi^- + \overline{\Xi}^+$.

3.5.3 *Systematic uncertainties for Λ and $\overline{\Lambda}$ due to feed-down*

Some of the reconstructed Λ and $\overline{\Lambda}$ particles come from decays of Ξ-hyperons. The proportion of reconstructed secondary Λ and $\overline{\Lambda}$ depends on the selection criteria used. For the parameters listed in Table 2 (V0 vertex part), the impact of the Ξ feed-down on the final spectra is evaluated to be 13% for Λ and 12% for $\overline{\Lambda}$. No p_T dependence is found within uncertainties.

This assessment results in a global correction of the spectra, applied as an additional factor in the overall normalization. Provided that both primary and secondary Λ have similar spectral shapes, such integrated correction is applicable. This is tested directly using Monte Carlo data, but also with real data, changing the fraction of the secondary Λ by varying the DCA of reconstructed candidates. Within the available statistics and p_T reach, no significant change in spectral shape is observed.

Using Monte Carlo, the ratio $r_{\text{feed-down}}$ of the reconstructed Ξ^- ($\overline{\Xi}^+$) candidates to the number of reconstructed Λ ($\overline{\Lambda}$) candidates from Ξ decays is:

$$r_{\text{feed-down}} = \frac{(N_{\overline{\Xi}^-})_{\text{MC}}}{(N_{\Lambda \leftarrow \Xi^-})_{\text{MC}}}$$

Assuming that this ratio is the same in both Monte Carlo and data, the whole feed-down contribution to the spectra is estimated by dividing the number of reconstructed Ξ^- ($\overline{\Xi}^+$) in data by the ratio extracted from Monte Carlo:

$$(N_{\Lambda \leftarrow \Xi^-})_{\text{data}} = \frac{(N_{\overline{\Xi}^-})_{\text{data}}}{r_{\text{feed-down}}}$$

Besides the Ξ contribution, other sources may feed the Λ population resulting in additional systematic uncertainties. In Monte Carlo simulations, Λ particles possibly generated in the detector material induce
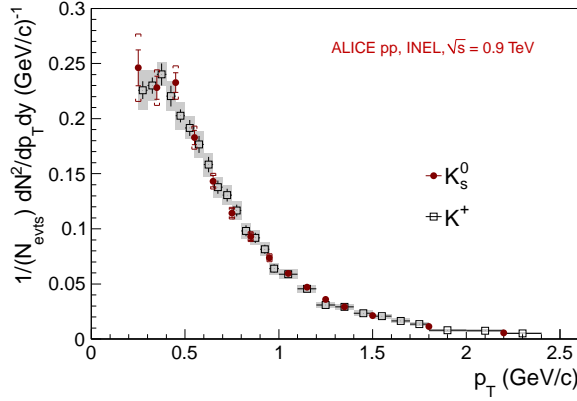
Fig. 13: Comparison of the corrected yields as a function of p_T for K_S^0 (circle) and charged kaons (K^+) (open squares), identified via energy loss in the TPC and ITS, and via time of flight in the TOF. The points are plotted at the centre of the bins. The full vertical lines associated to the K_S^0 points, as well as the gray shaded areas associated to the K^+ points, correspond to the statistical and systematic uncertainties summed in quadrature whereas the inner vertical lines contain only the statistical uncertainties (i.e. the number of reconstructed particles) and the systematics from the signal extraction.

a 1.7 % uncertainty. The same uncertainty in the case of $\overline{\Lambda}$ is below 1 %. The contribution from Ω decays is found to be negligible. It should be noted that since Λ ($\overline{\Lambda}$) from electromagnetic Σ^0 ($\overline{\Sigma}^0$) decays cannot be distinguished from the direct ones, the identified Λ ($\overline{\Lambda}$) include these contributions.

3.6 p_T spectra and global yield extraction

The K_S^0 spectrum is first shown on a linear scale in Fig. 13 and compared with charged kaon spectra [16]. Within uncertainties, good agreement is found between K_S^0 and K^+ in the measured p_T range.

Figure 14 presents the corrected p_T spectra for all species, including both statistical errors and systematic uncertainties. The spectra are fitted with two different functional forms in order to extract the global integrated yields:

$$\frac{d^2N}{dydp_T} = A \times p_T \times e^{-\frac{p_T}{T}} \tag{1}$$

$$\frac{d^2N}{dydp_T} = \frac{(n-1)(n-2)}{nT[nT+m(n-2)]} \times \frac{dN}{dy}$$
$$\times p_T \times \left(1 + \frac{m_T - m}{nT}\right)^{-n} \tag{2}$$

where $m_T = \sqrt{m^2 + p_T^2}$. The p_T exponential has two parameters: the normalization A and the inverse slope parameter T. The Lévy function [Eq. (2)], already used at lower energies [25], is shown to be useful when the p_T range is wide: it includes both an exponential shape for low p_T (which can be characterized by an inverse slope parameter T) and a power law component (governed by the power parameter n) for the higher p_T region. The results of these fits to the spectra, where statistical and systematic uncertainties are added in quadrature, are shown in Fig. 14 and in Table 5. In the case of K_S^0 for which the statistics and the p_T range are larger than for other species, the χ^2/NDF indicates clearly that the p_T exponential parameterization cannot properly reproduce the spectrum shape.

For the spectra of the ϕ, Λ and $\overline{\Lambda}$ both functions give similar and acceptable χ^2/NDF. Within uncertainties, Λ and $\overline{\Lambda}$ have the same fit parameters. In the case of the $\Xi^- + \overline{\Xi}^+$ spectrum, the low number (i.e. 3) of p_T bins cannot constrain the Lévy function and therefore its χ^2/NDF in Table 5 is not defined. Nevertheless, for consistency and in order to extract particle ratios, a Lévy fit is performed to

18

Table 5: Summary of the parameters extracted from the fits to the measured transverse momenta spectra using p_T exponential (1) and Lévy (2) functional forms and including point-to-point systematic uncertainties.

Particles		p_T exponential (1)		Lévy (2)		
		T (MeV)	χ^2/NDF	T (MeV)	n	χ^2/NDF
Mesons	K_S^0	325 ± 4	$117.6/14$	168 ± 5	6.6 ± 0.3	$10.8/13$
	ϕ	438 ± 31	$1.3/2$	164 ± 91	4.2 ± 2.5	$0.6/1$
Baryons	Λ	392 ± 6	$10.2/7$	229 ± 15	10.8 ± 2.0	$9.6/6$
	$\overline{\Lambda}$	385 ± 6	$5.1/7$	210 ± 15	9.2 ± 1.4	$3.7/6$
	$\Xi^- + \overline{\Xi}^+$	421 ± 42	$2.0/1$	175 ± 50	5.2 ± 2.3	$--$
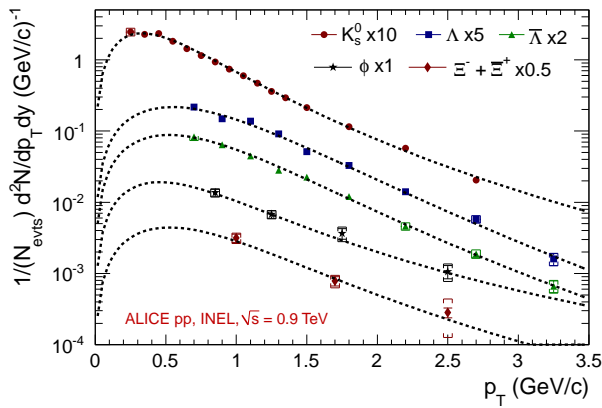
Fig. 14: Particle spectra (corrected yields) as a function of p_T for K_S^0 (circles), Λ (squares), $\overline{\Lambda}$ (triangles), ϕ (stars) and $\Xi^- + \overline{\Xi}^+$ (diamonds). The data points are scaled for visibility and plotted at the centre of the bins. Uncertainties corresponding to both statistics (i.e. the number of reconstructed particles) and systematics from the signal extraction are shown as vertical error bars. Statistical uncertainties and systematics (summarized in Table 4) added in quadrature are shown as brackets. The fits (dotted curves) using Lévy functional form [see Eq. (2)] are superimposed.

obtain the integrated yields and particle ratios for all species. It must be noted that the rapidity range is slightly different for each species (cf. Table 6). However, the rapidity dependence of particle production at mid-rapidity is weak enough to allow direct comparisons of the spectra [22].

4   Results and discussion

The p_T spectra for K_S^0, Λ, $\overline{\Lambda}$ and ϕ are shown in Fig. 14 along with the Lévy fits. When comparing the different spectra, it is found that the inverse slope parameter T increases with the mass of the particle. For example, it changes from 168 ± 5 MeV for K_S^0 to 229 ± 15 MeV for Λ when the Lévy fit is used. The $\Xi^- + \overline{\Xi}^+$ apparently do not follow this trend. However, this is most likely because the very limited statistics do not allow for a well-constrained fit. The shapes of the p_T spectra are also compared to PHO-JET and PYTHIA models. For PYTHIA, several tunes (109 [20], 306 [26] and 320 [27]) are presented. For all species, the p_T spectra are found to be slightly harder (i.e. they have a slower decrease with p_T) than the models as presented in Figs. 15, 16, 17 and 18. For transverse momenta larger than ~ 1 GeV/c, the strange particle spectra are strongly underestimated by all models, by a factor of ~ 2 for K_S^0 and even ~ 3 for hyperons. The discrepancy is smaller in the case of the ϕ.

The integrated yields (dN/dy) are obtained using the spectra in the measured range and integrating the
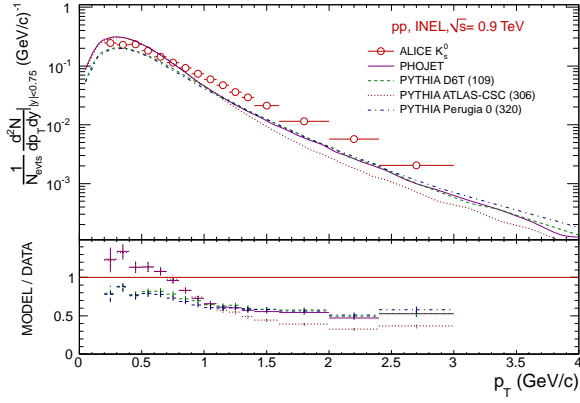
Fig. 15: Comparison of the transverse momentum differential yield for the K_S^0 particles for INEL pp collisions with PHOJET and PYTHIA tunes 109, 306 and 320.
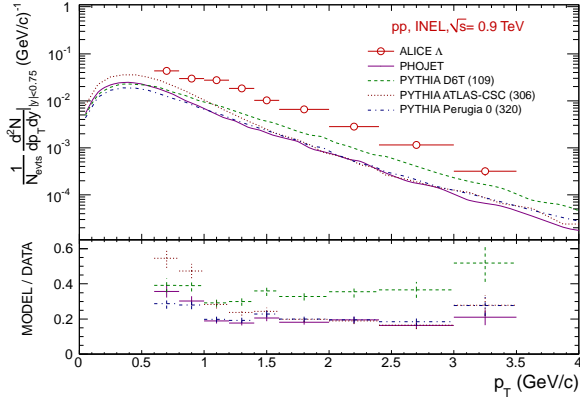
Fig. 16: Comparison of the transverse momentum differential yield for the Λ particles for INEL pp collisions with PHOJET and PYTHIA tunes 109, 306 and 320.

Fig. 17: Comparison of the transverse momentum differential yield for the ϕ particle for INEL pp collisions with PHOJET and PYTHIA tunes 109, 306 and 320.

Fig. 18: Comparison of the transverse momentum differential yield for the $\Xi^- + \overline{\Xi}^+$ particle for INEL pp collisions with PHOJET and PYTHIA tunes 109, 306 and 320.

Table 6: Rapidity and p_T ranges, $\langle p_T \rangle$, corrected yields and extrapolated fraction at low p_T using the Lévy function (2).

	Particles	$|y|$	p_T range (GeV/c)	$\langle p_T \rangle$ (GeV/c)	dN/dy	Extrapolation (%)
Mesons	K_S^0	< 0.75	$[0.2 - 3.0]$	$0.65 \pm 0.01 \pm 0.01$	$0.184 \pm 0.002 \pm 0.006$	$12 \pm 0.4 \pm 0.5$
	ϕ	< 0.60	$[0.7 - 3.0]$	$1.00 \pm 0.14 \pm 0.20$	$0.021 \pm 0.004 \pm 0.003$	$48 \pm 18 \pm 7$
Baryons	Λ	< 0.75	$[0.6 - 3.5]$	$0.86 \pm 0.01 \pm 0.01$	$0.048 \pm 0.001 \pm 0.004$	$36 \pm 2 \pm 4$
	$\overline{\Lambda}$	< 0.75	$[0.6 - 3.5]$	$0.84 \pm 0.02 \pm 0.02$	$0.047 \pm 0.002 \pm 0.005$	$39 \pm 3 \pm 4$
	$\Xi^- + \overline{\Xi}^+$	< 0.8	$[0.6 - 3.0]$	$0.95 \pm 0.14 \pm 0.03$	$0.0101 \pm 0.0020 \pm 0.0009$	$35 \pm 8 \pm 4$

Lévy function for the extrapolated regions at low and high p_T. The uncertainties for the dN/dy and $\langle p_T \rangle$ values are computed from the errors on the fit parameters, where both the point-to-point statistical and systematic uncertainties of the p_T spectra are taken into account. Due to the rapid decrease of the spectra, most of the extrapolation is done in the low p_T region and amounts to 12 % for K_S^0 and 48 % for the ϕ (smallest and highest values respectively). Therefore, an additional uncertainty is added for the dN/dy to account for the uncertainty in the shape of the spectra outside the measured range: it corresponds to 25% of the extrapolated particle yields at low p_T. The measured p_T ranges are specified in Table 6 for each particle species.

Using the particle integrated yields presented in this paper along with the yields of charged π, K, p and $\bar{p}$ [16] and the measured $\bar{p}$/p ratio [22], a comparison with STAR feed-down corrected particle ratios at $\sqrt{s} = 0.2$ TeV [25] is shown in Fig. 19. With the centre of mass energy increasing from $\sqrt{s} = 0.2$ TeV to 0.9 TeV the measured ratios are similar except the $\bar{p}/\pi^-$ ratio which decreases slightly from 0.068 ± 0.011 to 0.051 ± 0.005. The strange to non-strange particle ratios seem to increase but stay compatible within uncertainties: the K^-/π^- from 0.101 ± 0.012 to 0.121 ± 0.013 and the $\overline{\Lambda}/\pi^+$ from 0.027 ± 0.004 to 0.032 ± 0.003.

The yields and $\langle p_T \rangle$ obtained with the ALICE experiment are compared for each particle with existing data at the same energy and also with results at lower and higher energies. The various experiments differ in acceptance and event selection (i.e. NSD or INEL) but the dependence of $\langle p_T \rangle$ with respect to these variables is found to be negligible. Consequently the $\langle p_T \rangle$ values are directly comparable, whereas the comparison of the yields can require further scaling because of different (pseudo)rapidity coverages. Figure 20 reports ALICE $\langle p_T \rangle$ measurements along with those of the STAR experiment [25, 28]. It is remarkable that the $\langle p_T \rangle$ remains close to the ISR parameterization [29] although the collision energy
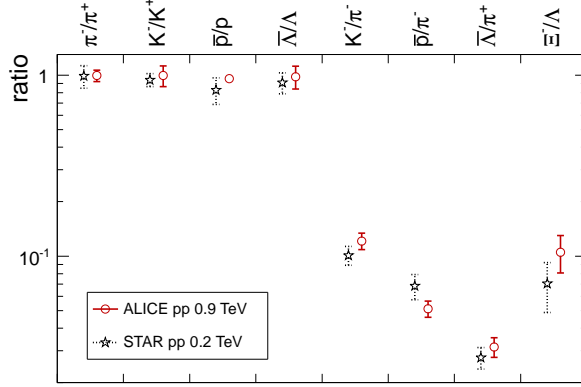
Fig. 19: Ratios of integrated yields including $\pi^{(\pm)}$, $K^{(\pm)}$, p and $\overline{p}$ performed with the ALICE experiment [16, 22] and compared with STAR values for pp collisions at $\sqrt{s} = 0.2$ TeV [25]. All ratios are feed-down corrected. For the ratio Ξ^-/Λ of ALICE, the $dN/dy|_{y=0}$ for $\Xi^- + \overline{\Xi}^+$ is divided by 2. Statistical and systematic uncertainties are added in quadrature.
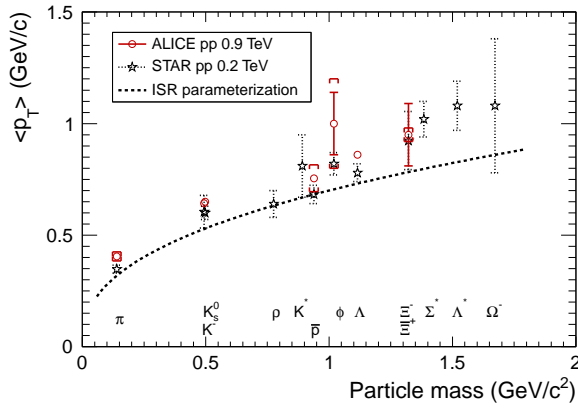
Fig. 20: $\langle p_T \rangle$ vs. particle mass for the measurements performed with the ALICE experiment and compared with STAR values for pp collisions at $\sqrt{s} = 0.2$ TeV [25, 28] and the ISR parameterization [29]. Both statistical (vertical error bars) and systematic (brackets) uncertainties are shown for ALICE data.

Table 7: The K_S^0 mean transverse momentum and yields in INEL events from UA5, CDF, and ALICE and in NSD events in STAR for various $\sqrt{s}$. STAR results are taken from [25], CDF ones and yield values with "*" are from [31]. Other UA5 values concerning $\langle p_T \rangle$ are from [30].

Experiment	$\sqrt{s}$ (GeV)	acceptance	$\langle p_T \rangle$ (GeV/c)	$dN/dy\|_{y=0}$
STAR	200	$\|y\| < 0.5$	0.61 ± 0.02	0.134 ± 0.011
UA5	200	$\|y\| < 2.5$	0.53 ± 0.07	$0.14 \pm 0.02^*$
UA5	546	$\|y\| < 2.5$	0.57 ± 0.03	$0.15 \pm 0.02^*$
CDF	630	$\|y\| < 1.0$	0.5 ± 0.1	$0.2 \pm 0.1^*$
UA5	900	$\|y\| < 2.5$	0.62 ± 0.08	$0.18 \pm 0.02^*$
ALICE	900	$\|y\| < 0.75$	$0.65 \pm 0.01 \pm 0.01$	$0.184 \pm 0.002 \pm 0.006$
CDF	1800	$\|y\| < 1.0$	0.60 ± 0.03	$0.26 \pm 0.03^*$

Table 8: The $(\Lambda + \overline{\Lambda})$ mean transverse momentum and yields for NSD events and different $\sqrt{s}$. STAR results are from [25] and UA5 results are from [32, 33]. ALICE and STAR results are feed-down corrected. The yield measured by ALICE has been scaled to match UA5 acceptance ($\|y\| < 2.0$) using the method explained in section 4.

Experiment	$\sqrt{s}$ (GeV)	acceptance	$\langle p_T \rangle$ (GeV/c)	$dN/dy\|_{y=0}$	$\langle n_{\Lambda+\overline{\Lambda}} \rangle$ per event	
					measured	scaled to UA5 $\|y\|$
STAR	200	$\|y\| < 0.5$	0.77 ± 0.04	0.074 ± 0.005	—	0.24 ± 0.02
UA5	200	$\|y\| < 2.0$	$0.80^{+0.20}_{-0.14}$	—	0.27 ± 0.07	—
UA5	546	$\|y\| < 2.0$	0.62 ± 0.08	—	0.25 ± 0.05	—
UA5	900	$\|y\| < 2.0$	0.74 ± 0.09	—	0.38 ± 0.08	—
ALICE	900	$\|y\| < 0.75$	$0.85 \pm 0.01 \pm 0.01$	$0.095 \pm 0.002 \pm 0.003$	—	$0.46 \pm 0.01 \pm 0.02$

increased by a factor 36. Table 7 summarizes the K_S^0 measurements performed by the UA5 [30], CDF [31] and ALICE Collaborations for INEL events, and by the STAR [25] Collaboration for NSD events. The ALICE K_S^0 yield at central rapidity, as well as the $\langle p_T \rangle$, are in good agreement with UA5 results at 900 GeV albeit with improved precision. The comparison of $(\Lambda + \overline{\Lambda})$ measurements are presented in Table 8 for NSD events. ALICE yields, measured in $|y| < 0.75$ for INEL events, are scaled to the UA5 [32, 33] acceptance ($|y| < 2.0$) using PYTHIA simulations. The $\Lambda + \overline{\Lambda}$ yield in NSD events is estimated by scaling the measured yield in inelastic events with the known ratio R of charged particle multiplicities in NSD and INEL events:

$$ R = \frac{(dN/dy)_{N_{ch}\text{NSD}}}{(dN/dy)_{N_{ch}\text{INEL}}} = 0.830 \pm 0.024 $$

This scaling factor is also used for the ALICE $(\Xi^- + \overline{\Xi}^+)$ yield presented in Table 9. The ALICE yields and $\langle p_T \rangle$ for both $(\Lambda + \overline{\Lambda})$ and $(\Xi^- + \overline{\Xi}^+)$ are in good agreement with the UA5 measurements [33]. Table 10 shows the evolution of dN/dy and $\langle p_T \rangle$ with the collision energy for the ϕ particle in NSD events. It includes the ALICE measurements, which are the first ϕ measurements at 900 GeV, and compares them to the results from the STAR experiment [34, 35] at 200 GeV and the E735 experiment [36] at 1800 GeV.

The baryon to meson ratio as a function of p_T obtained with the $(\Lambda + \overline{\Lambda})$ and K_S^0 spectra measured by ALICE is presented in Fig. 21. It includes the $(\Lambda + \overline{\Lambda})/2K_S^0$ ratio in pp collisions at 200 GeV measured by STAR [25], and the ratios in p$\overline{p}$ collisions at 630 GeV and 1800 GeV computed with the $(\Lambda + \overline{\Lambda})$ and K_S^0 spectra published by CDF [37] and UA1 [38]. UA1 and CDF Collaborations provide inclusive

Table 9: The $(\Xi^- + \overline{\Xi}^+)$ mean transverse momentum and yields for NSD events and different $\sqrt{s}$. STAR results are from [25] and UA5 results are from [33]. UA5 measures $(\Xi^- + \overline{\Xi}^+)$ for $p_T > 1$ GeV/c. The ALICE yield has been scaled to match the UA5 acceptance ($|y| < 3.0$) using the method explained in section 4.

Experiment	$\sqrt{s}$ (GeV)	acceptance	$\langle p_T \rangle$ (GeV/c)	dN/d$y|_{y=0}$	$\langle n_{\Xi^- + \overline{\Xi}^+} \rangle$ per event	
					measured	scaled to UA5 $|y|$
STAR	200	$|y| < 0.5$	0.90 ± 0.01	0.006 ± 0.001	—	0.022 ± 0.006
UA5	200	$|y| < 3.0$	$0.80^{+0.20}_{-0.14}$	—	$0.03^{+0.04}_{-0.02}$	—
UA5	546	$|y| < 3.0$	1.10 ± 0.02	—	$0.08^{+0.03}_{-0.02}$	—
UA5	900	$|y| < 3.0$	$0.7^{+0.2}_{-0.1}$	—	$0.05^{+0.04}_{-0.02}$	—
ALICE	900	$|y| < 0.8$	$0.95 \pm 0.14 \pm 0.03$	$0.0101 \pm 0.0020 \pm 0.0009$		$0.078 \pm 0.015 \pm 0.007$

Table 10: The ϕ mean transverse momentum and yields for NSD events and different $\sqrt{s}$. STAR results are from [34, 35] and E735 results are from [36]. The E735 Collaboration provided two values of $\langle p_T \rangle$ depending on the functional form used to fit the data points and the uncertainties associated with each value are only statistical. ALICE yields measured for INEL events have been scaled to NSD as explained in section 4.

Experiment	$\sqrt{s}$ (GeV)	acceptance	$\langle p_T \rangle$ (GeV/c)	dN/d$y|_{y=0}$
STAR	200	$|y| < 0.5$	$0.82 \pm 0.03 \pm 0.04$	$0.018 \pm 0.001 \pm 0.003$
ALICE	900	$|y| < 0.6$	$1.00 \pm 0.14 \pm 0.20$	$0.021 \pm 0.004 \pm 0.003$
E735	1800	$-0.4 < y < 1.0$	1.06 ± 0.18 0.94 ± 0.26	0.0186 ± 0.0041
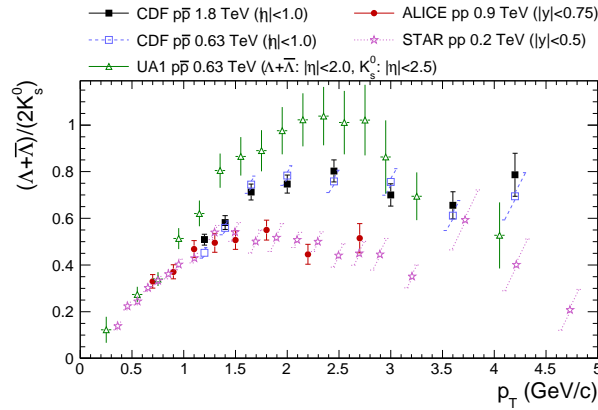
Fig. 21: $(\Lambda + \overline{\Lambda})/2K_S^0$ as a function of p_T for different collision energies in pp and p$\overline{p}$ minimum bias events. The STAR ratio is taken from [25] whereas the CDF and UA1 ratios are computed with the $(\Lambda + \overline{\Lambda})$ and K_S^0 spectra published in [37] and [38] respectively. The ALICE and STAR ratios are feed-down corrected. Because the K_S^0 and $(\Lambda + \overline{\Lambda})$ spectra from UA1 have incompatible binning, the K_S^0 differential yield has been calculated for each $(\Lambda + \overline{\Lambda})$ p_T data point using the fit function published by UA1. Such a choice is motivated by the fact that the χ^2 value for the K_S^0 spectrum fit is better than that for the $(\Lambda + \overline{\Lambda})$ spectrum.

spectra. The associated ratios are therefore not feed-down corrected, unlike the ALICE and STAR ones. The acceptance windows of these experiments differ significantly: ALICE measures Λ, $\overline{\Lambda}$ and K_S^0 in $|y| < 0.75$, STAR in $|y| < 0.5$, CDF in $|\eta| < 1.0$, whereas UA1 reconstructs $(\Lambda + \overline{\Lambda})$ in $|\eta| < 2.0$ and K_S^0 in $|\eta| < 2.5$. The ALICE ratio agrees very well with the STAR results in the measured p_T range, which would suggest little or no energy dependence of $(\Lambda + \overline{\Lambda})/2K_S^0$. A similar conclusion can be drawn when comparing only the ratios measured by CDF at 630 GeV and 1800 GeV, although the ratio found by CDF for $p_T > 1.5$ GeV/c is higher than the one observed with ALICE and STAR. The ratio computed from UA1 spectra however shows a clear disagreement with the other measurements in an intermediate p_T range between $p_T \approx 1.5$ GeV/c and $p_T \approx 3.0$ GeV/c. PYTHIA simulations show that this discrepancy can not be attributed to the differences in the acceptance or in the colliding system (i.e. p$\overline{p}$ instead of pp).

5   Conclusions

Measurements of mesons containing strange quarks (K_S^0 and ϕ) and hyperons (Λ, $\overline{\Lambda}$ and $\Xi^- + \overline{\Xi}^+$) have been performed for inelastic pp collisions at $\sqrt{s} = 0.9$ TeV with the ALICE experiment at the LHC. The Lévy function gives a good description of the transverse momentum spectra which have been compared with pQCD-based models. The K_S^0 transverse momentum spectrum is overestimated by PYTHIA tune ATLAS-CSC and PHOJET below 0.75 GeV/c but is higher by a factor of ~ 2 in the p_T range $[1 - 3]$ GeV/c. Within uncertainties, the ϕ meson spectrum is reasonably described by these models and the best agreement is obtained by PYTHIA tune D6T. We find that strange baryons are significantly under-predicted in both PYTHIA and PHOJET by a factor of ~ 3. The feed-down corrected ratio of baryon to meson as a function of p_T, illustrated by the Λ/K_S^0, is consistent with the STAR measurements at $\sqrt{s} = 0.2$ TeV but lower than UA1 and CDF results at $\sqrt{s} = 0.63$ TeV and $\sqrt{s} = 1.8$ TeV. The integrated yields and average transverse momenta have been compared with earlier data collected in pp and p$\overline{p}$ interactions at various energies. These results provide a useful baseline for comparisons with recent tunes of the PYTHIA model and a reference for future measurements in heavy-ion collisions at the LHC. These studies demonstrate the precision with which ALICE can measure resonances and topologically reconstructed weakly decaying particles. Measurements of these particles will be a substantial part of the ALICE programme in both pp and Pb–Pb collisions. The measurement of the ϕ resonance provides an unprecedented reference at this energy.

Acknowledgements

A The ALICE Collaboration

K. Aamodt[1] , A. Abrahantes Quintana[2] , D. Adamová[3] , A.M. Adare[4] , M.M. Aggarwal[5] , G. Aglieri Rinella[6] , A.G. Agocs[7] , S. Aguilar Salazar[8] , Z. Ahammed[9] , N. Ahmad[10] , A. Ahmad Masoodi[10] , S.U. Ahn[11],[i] , A. Akindinov[12] , D. Aleksandrov[13] , B. Alessandro[14] , R. Alfaro Molina[8] , A. Alici[15],[ii] , A. Alkin[16] , E. Almaráz Aviña[8] , T. Alt[17] , V. Altini[18] , S. Altinpinar[19] , I. Altsybeev[20] , C. Andrei[21] , A. Andronic[19] , V. Anguelov[22],[iii,iv] , C. Anson[23] , T. Antičić[24] , F. Antinori[25] , P. Antonioli[26] , L. Aphecetche[27] , H. Appelshäuser[28] , N. Arbor[29] , S. Arcelli[15] , A. Arend[28] , N. Armesto[30] , R. Arnaldi[14] , T. Aronsson[4] , I.C. Arsene[19] , A. Asryan[20] , A. Augustinus[6] , R. Averbeck[19] , T.C. Awes[31] , J. Äystö[32] , M.D. Azmi[10] , M. Bach[17] , A. Badalà[33] , Y.W. Baek[11],[i] , S. Bagnasco[14] , R. Bailhache[28] , R. Bala[34],[v] , R. Baldini Ferroli[35] , A. Baldisseri[36] , A. Baldit[37] , J. Bán[38] , R. Barbera[39] , F. Barile[18] , G.G. Barnaföldi[7] , L.S. Barnby[40] , V. Barret[37] , J. Bartke[41] , M. Basile[15] , N. Bastid[37] , B. Bathen[42] , G. Batigne[27] , B. Batyunya[43] , C. Baumann[28] , I.G. Bearden[44] , H. Beck[28] , I. Belikov[45] , F. Bellini[15] , R. Bellwied[46],[vi] , E. Belmont-Moreno[8] , S. Beole[34] , I. Berceanu[21] , A. Bercuci[21] , E. Berdermann[19] , Y. Berdnikov[47] , L. Betev[6] , A. Bhasin[48] , A.K. Bhati[5] , L. Bianchi[34] , N. Bianchi[49] , C. Bianchin[25] , J. Bielčík[50] , J. Bielčíková[3] , A. Bilandzic[51] , E. Biolcati[34] , A. Blanc[37] , F. Blanco[52] , F. Blanco[53] , D. Blau[13] , C. Blume[28] , M. Boccioli[6] , N. Bock[23] , A. Bogdanov[54] , H. Bøggild[44] , M. Bogolyubsky[55] , L. Boldizsár[7] , M. Bombara[56] , C. Bombonati[25] , J. Book[28] , H. Borel[36] , C. Bortolin[25],[vii] , S. Bose[57] , F. Bossú[34] , M. Botje[51] , S. Böttger[22] , B. Boyer[58] , P. Braun-Munzinger[19] , L. Bravina[59] , M. Bregant[60],[viii] , T. Breitner[22] , M. Broz[61] , R. Brun[6] , E. Bruna[4] , G.E. Bruno[18] , D. Budnikov[62] , H. Buesching[28] , O. Busch[63] , Z. Buthelezi[64] , D. Caffarri[25] , X. Cai[65] , H. Caines[4] , E. Calvo Villar[66] , P. Camerini[60] , V. Canoa Roman[6],[ix,x] , G. Cara Romeo[26] , F. Carena[6] , W. Carena[6] , F. Carminati[6] , A. Casanova Díaz[49] , M. Caselle[6] , J. Castillo Castellanos[36] , V. Catanescu[21] , C. Cavicchioli[6] , P. Cerello[14] , B. Chang[32] , S. Chapeland[6] , J.L. Charvet[36] , S. Chattopadhyay[57] , S. Chattopadhyay[9] , M. Cherney[67] , C. Cheshkov[68] , B. Cheynis[68] , E. Chiavassa[14] , V. Chibante Barroso[6] , D.D. Chinellato[69] , P. Chochula[6] , M. Chojnacki[70] , P. Christakoglou[70] , C.H. Christensen[44] , P. Christiansen[71] , T. Chujo[72] , C. Cicalo[73] , L. Cifarelli[15] , F. Cindolo[26] , J. Cleymans[64] , F. Coccetti[35] , J.-P. Coffin[45] , S. Coli[14] , G. Conesa Balbastre[49],[xi] , Z. Conesa del Valle[27],[xii] , P. Constantin[63] , G. Contin[60] , J.G. Contreras[74] , T.M. Cormier[46] , Y. Corrales Morales[34] , I. Cortés Maldonado[75] , P. Cortese[76] , M.R. Cosentino[69] , F. Costa[6] , M.E. Cotallo[52] , E. Crescio[74] , P. Crochet[37] , E. Cuautle[77] , L. Cunqueiro[49] , G. D Erasmo[18] , A. Dainese[78],[xiii] , H.H. Dalsgaard[44] , A. Danu[79] , D. Das[57] , I. Das[57] , A. Dash[80] , S. Dash[14] , S. De[9] , A. De Azevedo Moregula[49] , G.O.V. de Barros[81] , A. De Caro[82] , G. de Cataldo[83] , J. de Cuveland[17] , A. De Falco[84] , D. De Gruttola[82] , N. De Marco[14] , S. De Pasquale[82] , R. De Remigis[14] , R. de Rooij[70] , H. Delagrange[27] , Y. Delgado Mercado[66] , G. Dellacasa[76],[xiv] , A. Deloff[85] , V. Demanov[62] , E. Dénes[7] , A. Deppman[81] , D. Di Bari[18] , C. Di Giglio[18] , S. Di Liberto[86] , A. Di Mauro[6] , P. Di Nezza[49] , T. Dietel[42] , R. Divià[6] , Ø. Djuvsland[1] , A. Dobrin[46],[xv] , T. Dobrowolski[85] , I. Domínguez[77] , B. Dönigus[19] , O. Dordic[59] , O. Driga[27] , A.K. Dubey[9] , L. Ducroux[68] , P. Dupieux[37] , A.K. Dutta Majumdar[57] , M.R. Dutta Majumdar[9] , D. Elia[83] , D. Emschermann[42] , H. Engel[22] , H.A. Erdal[87] , B. Espagnon[58] , M. Estienne[27] , S. Esumi[72] , D. Evans[40] , S. Evrard[6] , G. Eyyubova[59] , C.W. Fabjan[6],[xvi] , D. Fabris[88] , J. Faivre[29] , D. Falchieri[15] , A. Fantoni[49] , M. Fasel[19] , R. Fearick[64] , A. Fedunov[43] , D. Fehlker[1] , V. Fekete[61] , D. Felea[79] , G. Feofilov[20] , A. Fernández Téllez[75] , A. Ferretti[34] , R. Ferretti[76],[xvii] , M.A.S. Figueredo[81] , S. Filchagin[62] , R. Fini[83] , D. Finogeev[89] , F.M. Fionda[18] , E.M. Fiore[18] , M. Floris[6] , S. Foertsch[64] , P. Foka[19] , S. Fokin[13] , E. Fragiacomo[90] , M. Fragkiadakis[91] , U. Frankenfeld[19] , U. Fuchs[6] , F. Furano[6] , C. Furget[29] , M. Fusco Girard[82] , J.J. Gaardhøje[44] , S. Gadrat[29] , M. Gagliardi[34] , A. Gago[66] , M. Gallio[34] , P. Ganoti[91],[xviii] , C. Garabatos[19] , R. Gemme[76] , J. Gerhard[17] , M. Germain[27] , C. Geuna[36] , A. Gheata[6] , M. Gheata[6] , B. Ghidini[18] , P. Ghosh[9] , M.R. Girard[92] , G. Giraudo[14] , P. Giubellino[34],[xix] , E. Gladysz-Dziadus[41] , P. Glässel[63] , R. Gomez[93] , L.H. González-Trueba[8] , P. González-Zamora[52] , H. González Santos[75] , S. Gorbunov[17] , S. Gotovac[94] , V. Grabski[8] , R. Grajcarek[63] , A. Grelli[70] , A. Grigoras[6] , C. Grigoras[6] , V. Grigoriev[54] , A. Grigoryan[95] , S. Grigoryan[43] , B. Grinyov[16] , N. Grion[90] , P. Gros[71] , J.F. Grosse-Oetringhaus[6] , J.-Y. Grossiord[68] , R. Grosso[88] , F. Guber[89] , R. Guernane[29] , C. Guerra Gutierrez[66] , B. Guerzoni[15] , K. Gulbrandsen[44] , T. Gunji[96] , A. Gupta[48] , R. Gupta[48] , H. Gutbrod[19] , Ø. Haaland[1] , C. Hadjidakis[58] , M. Haiduc[79] , H. Hamagaki[96] , G. Hamar[7] , J.W. Harris[4] , M. Hartig[28] , D. Hasch[49] , D. Hasegan[79] , D. Hatzifotiadou[26] , A. Hayrapetyan[95],[xvii] , M. Heide[42] , H. Heinz[4] , H. Helstrup[87] , A. Herghelegiu[21] , C. Hernández[19] , G. Herrera Corral[74] , N. Herrmann[63] , K.F. Hetland[87] , B. Hicks[4] , P.T. Hille[4] , B. Hippolyte[45] , T. Horaguchi[72] , Y. Hori[96] , P. Hristov[6] , I. Hřivnáčová[58] , M. Huang[1] , S. Huber[19] , T.J. Humanic[23] , D.S. Hwang[97] , R. Ichou[27] , R. Ilkaev[62] , I. Ilkiv[85] , M. Inaba[72] , E. Incani[84] , G.M. Innocenti[34] , P.G. Innocenti[6] , M. Ippolitov[13] , M. Irfan[10] , C. Ivan[19] , A. Ivanov[20] , M. Ivanov[19] , V. Ivanov[47] , A. Jachołkowski[6] , P.M. Jacobs[98] , L. Jancurová[43] , S. Jangal[45] , R. Janik[61] , S.P. Jayarathna[53],[xx] , S. Jena[99] , L. Jirden[6] , G.T. Jones[40] , P.G. Jones[40] , P. Jovanović[40] , H. Jung[11] , W. Jung[11] , A. Jusko[40] , S. Kalcher[17] ,

P. Kaliňák[38], M. Kalisky[42], T. Kalliokoski[32], A. Kalweit[100], R. Kamermans[70],[xiv], K. Kanaki[1], E. Kang[11], J.H. Kang[101], V. Kaplin[54], O. Karavichev[89], T. Karavicheva[89], E. Karpechev[89], A. Kazantsev[13], U. Kebschull[22], R. Keidel[102], M.M. Khan[10], A. Khanzadeev[47], Y. Kharlov[55], B. Kileng[87], D.J. Kim[32], D.S. Kim[11], D.W. Kim[11], H.N. Kim[11], J.H. Kim[97], J.S. Kim[11], M. Kim[11], M. Kim[101], S. Kim[97], S.H. Kim[11], S. Kirsch[6],[xxi], I. Kisel[22],[iv], S. Kiselev[12], A. Kisiel[6], J.L. Klay[103], J. Klein[63], C. Klein-Bösing[42], M. Kliemant[28], A. Klovning[1], A. Kluge[6], M.L. Knichel[19], K. Koch[63], M.K. Köhler[19], R. Kolevatov[59], A. Kolojvari[20], V. Kondratiev[20], N. Kondratyeva[54], A. Konevskih[89], E. Kornaś[41], C. Kottachchi Kankanamge Don[46], R. Kour[40], M. Kowalski[41], S. Kox[29], G. Koyithatta Meethaleveedu[99], K. Kozlov[13], J. Kral[32], I. Králik[38], F. Kramer[28], I. Kraus[100],[xxii], T. Krawutschke[63],[xxiii], M. Kretz[17], M. Krivda[40],[xxiv], D. Krumbhorn[63], M. Krus[50], E. Kryshen[47], M. Krzewicki[51], Y. Kucheriaev[13], C. Kuhn[45], P.G. Kuijer[51], P. Kurashvili[85], A. Kurepin[89], A.B. Kurepin[89], A. Kuryakin[62], S. Kushpil[3], V. Kushpil[3], M.J. Kweon[63], Y. Kwon[101], P. La Rocca[39], P. Ladrón de Guevara[52],[xxv], V. Lafage[58], C. Lara[22], D.T. Larsen[1], C. Lazzeroni[40], Y. Le Bornec[58], R. Lea[60], K.S. Lee[11], S.C. Lee[11], F. Lefèvre[27], J. Lehnert[28], L. Leistam[6], M. Lenhardt[27], V. Lenti[83], I. León Monzón[93], H. León Vargas[28], P. Lévai[7], X. Li[104], R. Lietava[40], S. Lindal[59], V. Lindenstruth[22],[iv], C. Lippmann[6],[xxii], M.A. Lisa[23], L. Liu[1], V.R. Loggins[46], V. Loginov[54], S. Lohn[6], D. Lohner[63], C. Loizides[98], X. Lopez[37], M. López Noriega[58], E. López Torres[2], G. Løvhøiden[59], X.-G. Lu[63], P. Luettig[28], M. Lunardon[25], G. Luparello[34], L. Luquin[27], C. Luzzi[6], K. Ma[65], R. Ma[4], D.M. Madagodahettige-Don[53], A. Maevskaya[89], M. Mager[6], D.P. Mahapatra[80], A. Maire[45], M. Malaev[47], I. Maldonado Cervantes[77], D. Mal'Kevich[12], P. Malzacher[19], A. Mamonov[62], L. Manceau[37], L. Mangotra[48], V. Manko[13], F. Manso[37], V. Manzari[83], Y. Mao[65],[xxvi], J. Mareš[105], G.V. Margagliotti[60], A. Margotti[26], A. Marín[19], I. Martashvili[106], P. Martinengo[6], M.I. Martínez[75], A. Martínez Davalos[8], G. Martínez García[27], Y. Martynov[16], A. Mas[27], S. Masciocchi[19], M. Masera[34], A. Masoni[73], L. Massacrier[68], M. Mastromarco[83], A. Mastroserio[6], Z.L. Matthews[40], A. Matyja[41],[viii], D. Mayani[77], G. Mazza[14], M.A. Mazzoni[86], F. Meddi[107], A. Menchaca-Rocha[8], P. Mendez Lorenzo[6], J. Mercado Pérez[63], P. Mereu[14], Y. Miake[72], J. Midori[108], L. Milano[34], J. Milosevic[59],[xxvii], A. Mischke[70], D. Miśkowiec[19],[xix], C. Mitu[79], J. Mlynarz[46], B. Mohanty[9], L. Molnar[6], L. Montaño Zetina[74], M. Monteno[14], E. Montes[52], M. Morando[25], D.A. Moreira De Godoy[81], S. Moretto[25], A. Morsch[6], V. Muccifora[49], E. Mudnic[94], H. Müller[6], S. Muhuri[9], M.G. Munhoz[81], J. Munoz[75], L. Musa[6], A. Musso[14], B.K. Nandi[99], R. Nania[26], E. Nappi[83], C. Nattrass[106], F. Navach[18], S. Navin[40], T.K. Nayak[9], S. Nazarenko[62], G. Nazarov[62], A. Nedosekin[12], F. Nendaz[68], J. Newby[109], M. Nicassio[18], B.S. Nielsen[44], S. Nikolaev[13], V. Nikolic[24], S. Nikulin[13], V. Nikulin[47], B.S. Nilsen[67], M.S. Nilsson[59], F. Noferini[26], G. Nooren[70], N. Novitzky[32], A. Nyanin[13], A. Nyatha[99], C. Nygaard[44], J. Nystrand[1], H. Obayashi[108], A. Ochirov[20], H. Oeschler[100], S.K. Oh[11], J. Oleniacz[92], C. Oppedisano[14], A. Ortiz Velasquez[77], G. Ortona[34], A. Oskarsson[71], P. Ostrowski[92], I. Otterlund[71], J. Otwinowski[19], G. Øvrebekk[1], K. Oyama[63], K. Ozawa[96], Y. Pachmayer[63], M. Pachr[50], F. Padilla[34], P. Pagano[82], G. Paić[77], F. Painke[17], C. Pajares[30], S. Pal[36], S.K. Pal[9], A. Palaha[40], A. Palmeri[33], G.S. Pappalardo[33], W.J. Park[19], V. Paticchio[83], A. Pavlinov[46], T. Pawlak[92], T. Peitzmann[70], D. Peresunko[13], C.E. Pérez Lara[51], D. Perini[6], D. Perrino[18], W. Peryt[92], A. Pesci[26], V. Peskov[6], Y. Pestov[110], A.J. Peters[6], V. Petráček[50], M. Petris[21], P. Petrov[40], M. Petrovici[21], C. Petta[39], S. Piano[90], A. Piccotti[14], M. Pikna[61], P. Pillot[27], O. Pinazza[6], L. Pinsky[53], N. Pitz[28], F. Piuz[6], D.B. Piyarathna[46],[xxviii], R. Platt[40], M. Płoskoń[98], J. Pluta[92], T. Pocheptsov[43],[xxix], S. Pochybova[7], P.L.M. Podesta-Lerma[93], M.G. Poghosyan[34], K. Polák[105], B. Polichtchouk[55], A. Pop[21], V. Pospíšil[50], B. Potukuchi[48], S.K. Prasad[46],[xxx], R. Preghenella[35], F. Prino[14], C.A. Pruneau[46], I. Pshenichnov[89], G. Puddu[84], A. Pulvirenti[39], V. Punin[62], M. Putiš[56], J. Putschke[4], E. Quercigh[6], H. Qvigstad[59], A. Rachevski[90], A. Rademakers[6], O. Rademakers[6], S. Radomski[63], T.S. Räihä[32], J. Rak[32], A. Rakotozafindrabe[36], L. Ramello[76], A. Ramírez Reyes[74], M. Rammler[42], R. Raniwala[111], S. Raniwala[111], S.S. Räsänen[32], K.F. Read[106], J.S. Real[29], K. Redlich[85], R. Renfordt[28], A.R. Reolon[49], A. Reshetin[89], F. Rettig[17], J.-P. Revol[6], K. Reygers[63], H. Ricaud[100], L. Riccati[14], R.A. Ricci[78], M. Richter[1],[xxxi], P. Riedler[6], W. Riegler[6], F. Riggi[39], A. Rivetti[14], M. Rodríguez Cahuantzi[75], D. Rohr[17], D. Röhrich[1], R. Romita[19], F. Ronchetti[49], P. Rosinský[6], P. Rosnet[37], S. Rossegger[6], A. Rossi[25], F. Roukoutakis[91], S. Rousseau[58], C. Roy[27],[xii], P. Roy[57], A.J. Rubio Montero[52], R. Rui[60], I. Rusanov[6], E. Ryabinkin[13], A. Rybicki[41], S. Sadovsky[55], K. Šafařík[6], R. Sahoo[25], P.K. Sahu[80], P. Saiz[6], S. Sakai[98], D. Sakata[72], C.A. Salgado[30], T. Samanta[9], S. Sambyal[48], V. Samsonov[47], L. Šándor[38], A. Sandoval[8], M. Sano[72], S. Sano[96], R. Santo[42], R. Santoro[83], J. Sarkamo[32], P. Saturnini[37], E. Scapparone[26], F. Scarlassara[25], R.P. Scharenberg[112], C. Schiaua[21], R. Schicker[63], C. Schmidt[19], H.R. Schmidt[19], S. Schreiner[6], S. Schuchmann[28], J. Schukraft[6], Y. Schutz[27],[xvii], K. Schwarz[19], K. Schweda[63], G. Scioli[15], E. Scomparin[14], P.A. Scott[40], R. Scott[106], G. Segato[25], S. Senyukov[76], J. Seo[11], S. Serci[84], E. Serradilla[52], A. Sevcenco[79], G. Shabratova[43], R. Shahoyan[6], N. Sharma[5], S. Sharma[48], K. Shigaki[108], M. Shimomura[72],

K. Shtejer[2], Y. Sibiriak[13], M. Siciliano[34], E. Sicking[6], T. Siemiarczuk[85], A. Silenzi[15], D. Silvermyr[31], G. Simonetti[6,xxxii], R. Singaraju[9], R. Singh[48], B.C. Sinha[9], T. Sinha[57], B. Sitar[61], M. Sitta[76], T.B. Skaali[59], K. Skjerdal[1], R. Smakal[50], N. Smirnov[4], R. Snellings[51,xxxiii], C. Søgaard[44], A. Soloviev[55], R. Soltz[109], H. Son[97], M. Song[101], C. Soos[6], F. Soramel[25], M. Spyropoulou-Stassinaki[91], B.K. Srivastava[112], J. Stachel[63], I. Stan[79], G. Stefanek[85], G. Stefanini[6], T. Steinbeck[22,iv], E. Stenlund[71], G. Steyn[64], D. Stocco[27], R. Stock[28], M. Stolpovskiy[55], P. Strmen[61], A.A.P. Suaide[81], M.A. Subieta Vásquez[34], T. Sugitate[108], C. Suire[58], M. Šumbera[3], T. Susa[24], D. Swoboda[6], T.J.M. Symons[98], A. Szanto de Toledo[81], I. Szarka[61], A. Szostak[1], C. Tagridis[91], J. Takahashi[69], J.D. Tapia Takaki[58], A. Tauro[6], M. Tavlet[6], G. Tejeda Muñoz[75], A. Telesca[6], C. Terrevoli[18], J. Thäder[19], D. Thomas[70], J.H. Thomas[19], R. Tieulent[68], A.R. Timmins[46,vi], D. Tlusty[50], A. Toia[6], H. Torii[108], L. Toscano[6], F. Tosello[14], T. Traczyk[92], D. Truesdale[23], W.H. Trzaska[32], A. Tumkin[62], R. Turrisi[88], A.J. Turvey[67], T.S. Tveter[59], J. Ulery[28], K. Ullaland[1], A. Uras[84], J. Urbán[56], G.M. Urciuoli[86], G.L. Usai[84], A. Vacchi[90], M. Vala[43,xxiv], L. Valencia Palomo[58], S. Vallero[63], N. van der Kolk[51], M. van Leeuwen[70], P. Vande Vyvre[6], L. Vannucci[78], A. Vargas[75], R. Varma[99], M. Vasileiou[91], A. Vasiliev[13], V. Vechernin[20], M. Venaruzzo[60], E. Vercellin[34], S. Vergara[75], R. Vernet[113], M. Verweij[70], L. Vickovic[94], G. Viesti[25], O. Vikhlyantsev[62], Z. Vilakazi[64], O. Villalobos Baillie[40], A. Vinogradov[13], L. Vinogradov[20], Y. Vinogradov[62], T. Virgili[82], Y.P. Viyogi[9], A. Vodopyanov[43], K. Voloshin[12], S. Voloshin[46], G. Volpe[18], B. von Haller[6], D. Vranic[19], J. Vrláková[56], B. Vulpescu[37], B. Wagner[1], V. Wagner[50], R. Wan[45,xxxiv], D. Wang[65], Y. Wang[63], Y. Wang[65], K. Watanabe[72], J.P. Wessels[42], U. Westerhoff[42], J. Wiechula[63], J. Wikne[59], M. Wilde[42], A. Wilk[42], G. Wilk[85], M.C.S. Williams[26], B. Windelband[63], H. Yang[36], S. Yasnopolskiy[13], J. Yi[114], Z. Yin[65], H. Yokoyama[72], I.-K. Yoo[114], X. Yuan[65], I. Yushmanov[13], E. Zabrodin[59], C. Zampolli[6], S. Zaporozhets[43], A. Zarochentsev[20], P. Závada[105], H. Zbroszczyk[92], P. Zelnicek[22], A. Zenin[55], I. Zgura[79], M. Zhalov[47], X. Zhang[65,i], D. Zhou[65], X. Zhu[65], A. Zichichi[15,xxxv], G. Zinovjev[16], Y. Zoccarato[68], M. Zynovyev[16]

Affiliation notes

i Also at Laboratoire de Physique Corpusculaire (LPC), Clermont Université, Université Blaise Pascal, CNRS–IN2P3, Clermont-Ferrand, France

ii Now at Centro Fermi – Centro Studi e Ricerche e Museo Storico della Fisica "Enrico Fermi", Rome, Italy

iii Now at Physikalisches Institut, Ruprecht-Karls-Universität Heidelberg, Heidelberg, Germany

iv Now at Frankfurt Institute for Advanced Studies, Johann Wolfgang Goethe-Universität Frankfurt, Frankfurt, Germany

v Now at Sezione INFN, Turin, Italy

vi Now at University of Houston, Houston, Texas, United States

vii Also at Dipartimento di Fisica dell'Universitá, Udine, Italy

viii Now at SUBATECH, Ecole des Mines de Nantes, Université de Nantes, CNRS-IN2P3, Nantes, France

ix Now at Centro de Investigación y de Estudios Avanzados (CINVESTAV), Mexico City and Mérida, Mexico

x Now at Benemérita Universidad Autónoma de Puebla, Puebla, Mexico

xi Now at Laboratoire de Physique Subatomique et de Cosmologie (LPSC), Université Joseph Fourier, CNRS-IN2P3, Institut Polytechnique de Grenoble, Grenoble, France

xii Now at Institut Pluridisciplinaire Hubert Curien (IPHC), Université de Strasbourg, CNRS-IN2P3, Strasbourg, France

xiii Now at Sezione INFN, Padova, Italy

xiv Deceased

xv Also at Division of Experimental High Energy Physics, University of Lund, Lund, Sweden

xvi Also at University of Technology and Austrian Academy of Sciences, Vienna, Austria

xvii Also at European Organization for Nuclear Research (CERN), Geneva, Switzerland

xviii Now at Oak Ridge National Laboratory, Oak Ridge, Tennessee, United States

xix Now at European Organization for Nuclear Research (CERN), Geneva, Switzerland

xx Also at Wayne State University, Detroit, Michigan, United States

xxi Also at Frankfurt Institute for Advanced Studies, Johann Wolfgang Goethe-Universität Frankfurt, Frankfurt, Germany

xxii Now at Research Division and ExtreMe Matter Institute EMMI, GSI Helmholtzzentrum für Schwerionenforschung, Darmstadt, Germany

xxiii Also at Fachhochschule Köln, Köln, Germany

xxiv Also at Institute of Experimental Physics, Slovak Academy of Sciences, Košice, Slovakia

[xxv] Now at Instituto de Ciencias Nucleares, Universidad Nacional Autónoma de México, Mexico City, Mexico

[xxvi] Also at Laboratoire de Physique Subatomique et de Cosmologie (LPSC), Université Joseph Fourier, CNRS-IN2P3, Institut Polytechnique de Grenoble, Grenoble, France

[xxvii] Also at "Vinča" Institute of Nuclear Sciences, Belgrade, Serbia

[xxviii] Also at University of Houston, Houston, Texas, United States

[xxix] Also at Department of Physics, University of Oslo, Oslo, Norway

[xxx] Also at Variable Energy Cyclotron Centre, Kolkata, India

[xxxi] Now at Department of Physics, University of Oslo, Oslo, Norway

[xxxii] Also at Dipartimento Interateneo di Fisica 'M. Merlin' and Sezione INFN, Bari, Italy

[xxxiii] Now at Nikhef, National Institute for Subatomic Physics and Institute for Subatomic Physics of Utrecht University, Utrecht, Netherlands

[xxxiv] Also at Hua-Zhong Normal University, Wuhan, China

[xxxv] Also at Centro Fermi – Centro Studi e Ricerche e Museo Storico della Fisica "Enrico Fermi", Rome, Italy

Collaboration Institutes

[1] Department of Physics and Technology, University of Bergen, Bergen, Norway

[2] Centro de Aplicaciones Tecnológicas y Desarrollo Nuclear (CEADEN), Havana, Cuba

[3] Nuclear Physics Institute, Academy of Sciences of the Czech Republic, Řež u Prahy, Czech Republic

[4] Yale University, New Haven, Connecticut, United States

[5] Physics Department, Panjab University, Chandigarh, India

[6] European Organization for Nuclear Research (CERN), Geneva, Switzerland

[7] KFKI Research Institute for Particle and Nuclear Physics, Hungarian Academy of Sciences, Budapest, Hungary

[8] Instituto de Física, Universidad Nacional Autónoma de México, Mexico City, Mexico

[9] Variable Energy Cyclotron Centre, Kolkata, India

[10] Department of Physics Aligarh Muslim University, Aligarh, India

[11] Gangneung-Wonju National University, Gangneung, South Korea

[12] Institute for Theoretical and Experimental Physics, Moscow, Russia

[13] Russian Research Centre Kurchatov Institute, Moscow, Russia

[14] Sezione INFN, Turin, Italy

[15] Dipartimento di Fisica dell'Università and Sezione INFN, Bologna, Italy

[16] Bogolyubov Institute for Theoretical Physics, Kiev, Ukraine

[17] Frankfurt Institute for Advanced Studies, Johann Wolfgang Goethe-Universität Frankfurt, Frankfurt, Germany

[18] Dipartimento Interateneo di Fisica 'M. Merlin' and Sezione INFN, Bari, Italy

[19] Research Division and ExtreMe Matter Institute EMMI, GSI Helmholtzzentrum für Schwerionenforschung, Darmstadt, Germany

[20] V. Fock Institute for Physics, St. Petersburg State University, St. Petersburg, Russia

[21] National Institute for Physics and Nuclear Engineering, Bucharest, Romania

[22] Kirchhoff-Institut für Physik, Ruprecht-Karls-Universität Heidelberg, Heidelberg, Germany

[23] Department of Physics, Ohio State University, Columbus, Ohio, United States

[24] Rudjer Bošković Institute, Zagreb, Croatia

[25] Dipartimento di Fisica dell'Università and Sezione INFN, Padova, Italy

[26] Sezione INFN, Bologna, Italy

[27] SUBATECH, Ecole des Mines de Nantes, Université de Nantes, CNRS-IN2P3, Nantes, France

[28] Institut für Kernphysik, Johann Wolfgang Goethe-Universität Frankfurt, Frankfurt, Germany

[29] Laboratoire de Physique Subatomique et de Cosmologie (LPSC), Université Joseph Fourier, CNRS-IN2P3, Institut Polytechnique de Grenoble, Grenoble, France

[30] Departamento de Física de Partículas and IGFAE, Universidad de Santiago de Compostela, Santiago de Compostela, Spain

[31] Oak Ridge National Laboratory, Oak Ridge, Tennessee, United States

[32] Helsinki Institute of Physics (HIP) and University of Jyväskylä, Jyväskylä, Finland

[33] Sezione INFN, Catania, Italy

[34] Dipartimento di Fisica Sperimentale dell'Università and Sezione INFN, Turin, Italy

[35] Centro Fermi – Centro Studi e Ricerche e Museo Storico della Fisica "Enrico Fermi", Rome, Italy

[36] Commissariat à l'Energie Atomique, IRFU, Saclay, France

[37] Laboratoire de Physique Corpusculaire (LPC), Clermont Université, Université Blaise Pascal, CNRS–IN2P3, Clermont-Ferrand, France

[38] Institute of Experimental Physics, Slovak Academy of Sciences, Košice, Slovakia

[39] Dipartimento di Fisica e Astronomia dell'Università and Sezione INFN, Catania, Italy

[40] School of Physics and Astronomy, University of Birmingham, Birmingham, United Kingdom

[41] The Henryk Niewodniczanski Institute of Nuclear Physics, Polish Academy of Sciences, Cracow, Poland

[42] Institut für Kernphysik, Westfälische Wilhelms-Universität Münster, Münster, Germany

[43] Joint Institute for Nuclear Research (JINR), Dubna, Russia

[44] Niels Bohr Institute, University of Copenhagen, Copenhagen, Denmark

[45] Institut Pluridisciplinaire Hubert Curien (IPHC), Université de Strasbourg, CNRS-IN2P3, Strasbourg, France

[46] Wayne State University, Detroit, Michigan, United States

[47] Petersburg Nuclear Physics Institute, Gatchina, Russia

[48] Physics Department, University of Jammu, Jammu, India

[49] Laboratori Nazionali di Frascati, INFN, Frascati, Italy

[50] Faculty of Nuclear Sciences and Physical Engineering, Czech Technical University in Prague, Prague, Czech Republic

[51] Nikhef, National Institute for Subatomic Physics, Amsterdam, Netherlands

[52] Centro de Investigaciones Energéticas Medioambientales y Tecnológicas (CIEMAT), Madrid, Spain

[53] University of Houston, Houston, Texas, United States

[54] Moscow Engineering Physics Institute, Moscow, Russia

[55] Institute for High Energy Physics, Protvino, Russia

[56] Faculty of Science, P.J. Šafárik University, Košice, Slovakia

[57] Saha Institute of Nuclear Physics, Kolkata, India

[58] Institut de Physique Nucléaire d'Orsay (IPNO), Université Paris-Sud, CNRS-IN2P3, Orsay, France

[59] Department of Physics, University of Oslo, Oslo, Norway

[60] Dipartimento di Fisica dell'Università and Sezione INFN, Trieste, Italy

[61] Faculty of Mathematics, Physics and Informatics, Comenius University, Bratislava, Slovakia

[62] Russian Federal Nuclear Center (VNIIEF), Sarov, Russia

[63] Physikalisches Institut, Ruprecht-Karls-Universität Heidelberg, Heidelberg, Germany

[64] Physics Department, University of Cape Town, iThemba Laboratories, Cape Town, South Africa

[65] Hua-Zhong Normal University, Wuhan, China

[66] Sección Física, Departamento de Ciencias, Pontificia Universidad Católica del Perú, Lima, Peru

[67] Physics Department, Creighton University, Omaha, Nebraska, United States

[68] Université de Lyon, Université Lyon 1, CNRS/IN2P3, IPN-Lyon, Villeurbanne, France

[69] Universidade Estadual de Campinas (UNICAMP), Campinas, Brazil

[70] Nikhef, National Institute for Subatomic Physics and Institute for Subatomic Physics of Utrecht University, Utrecht, Netherlands

[71] Division of Experimental High Energy Physics, University of Lund, Lund, Sweden

[72] University of Tsukuba, Tsukuba, Japan

[73] Sezione INFN, Cagliari, Italy

[74] Centro de Investigación y de Estudios Avanzados (CINVESTAV), Mexico City and Mérida, Mexico

[75] Benemérita Universidad Autónoma de Puebla, Puebla, Mexico

[76] Dipartimento di Scienze e Tecnologie Avanzate dell'Università del Piemonte Orientale and Gruppo Collegato INFN, Alessandria, Italy

[77] Instituto de Ciencias Nucleares, Universidad Nacional Autónoma de México, Mexico City, Mexico

[78] Laboratori Nazionali di Legnaro, INFN, Legnaro, Italy

[79] Institute of Space Sciences (ISS), Bucharest, Romania

[80] Institute of Physics, Bhubaneswar, India

[81] Universidade de São Paulo (USP), São Paulo, Brazil

[82] Dipartimento di Fisica 'E.R. Caianiello' dell'Università and Gruppo Collegato INFN, Salerno, Italy

[83] Sezione INFN, Bari, Italy

[84] Dipartimento di Fisica dell'Università and Sezione INFN, Cagliari, Italy

[85] Soltan Institute for Nuclear Studies, Warsaw, Poland

[86] Sezione INFN, Rome, Italy

[87] Faculty of Engineering, Bergen University College, Bergen, Norway

[88] Sezione INFN, Padova, Italy

[89] Institute for Nuclear Research, Academy of Sciences, Moscow, Russia

[90] Sezione INFN, Trieste, Italy

[91] Physics Department, University of Athens, Athens, Greece

[92] Warsaw University of Technology, Warsaw, Poland

[93] Universidad Autónoma de Sinaloa, Culiacán, Mexico

[94] Technical University of Split FESB, Split, Croatia

[95] Yerevan Physics Institute, Yerevan, Armenia

[96] University of Tokyo, Tokyo, Japan

[97] Department of Physics, Sejong University, Seoul, South Korea

[98] Lawrence Berkeley National Laboratory, Berkeley, California, United States

[99] Indian Institute of Technology, Mumbai, India

[100] Institut für Kernphysik, Technische Universität Darmstadt, Darmstadt, Germany

[101] Yonsei University, Seoul, South Korea

[102] Zentrum für Technologietransfer und Telekommunikation (ZTT), Fachhochschule Worms, Worms, Germany

[103] California Polytechnic State University, San Luis Obispo, California, United States

[104] China Institute of Atomic Energy, Beijing, China

[105] Institute of Physics, Academy of Sciences of the Czech Republic, Prague, Czech Republic

[106] University of Tennessee, Knoxville, Tennessee, United States

[107] Dipartimento di Fisica dell'Università 'La Sapienza' and Sezione INFN, Rome, Italy

[108] Hiroshima University, Hiroshima, Japan

[109] Lawrence Livermore National Laboratory, Livermore, California, United States

[110] Budker Institute for Nuclear Physics, Novosibirsk, Russia

[111] Physics Department, University of Rajasthan, Jaipur, India

[112] Purdue University, West Lafayette, Indiana, United States

[113] Centre de Calcul de l'IN2P3, Villeurbanne, France

[114] Pusan National University, Pusan, South Korea

References

[1] T. Sjöstrand, S. Mrenna and P. Z. Skands, J. High Energy Phys. 0605 (2006) 026.

[2] R. Engel, J. Ranft and S. Roesler, Phys. Rev. D**52**, (1995) 1459.

[3] F. Becattini and U. W. Heinz, Z. Phys. C**76**, (1997) 269.

[4] I. Kraus, J. Cleymans, H. Oeschler and K. Redlich, Phys. Rev. C**79**, (2009) 014901.

[5] F. Becattini, P. Castorina, A. Milov, and H. Satz, arXiv:0912.2855[hep-ph].

[6] T. Sjöstrand and P. Z. Skands, Eur. Phys. J. C**39**, (2005) 129.

[7] L. Evans and P. Bryant, (ed.), JINST **3**, (2008) S08001.

[8] ALICE Collaboration, K. Aamodt *et al.*, Eur. Phys. J. C**65**, (2010) 111.

[9] ALICE Collaboration, K. Aamodt *et al.*, Eur. Phys. J. C**68**, (2010) 89.

[10] ALICE Collaboration, K. Aamodt *et al.*, JINST 3 **64**, (2008) S08002.

[11] ALICE Collaboration, K. Aamodt *et al.*, JINST 5 (2010) P03003.

[12] J. Alme *et al.* Nucl. Instrum. Meth. A **622**, (2010) 316.

[13] A. Akindinov *et al.* Eur. Phys. J. **C68**, (2010) 601 and references therein.

[14] ALICE Collaboration, K. Aamodt *et al.*, Phys. Lett. B **693**, 53 (2010).

[15] ALICE Collaboration, B. Alessandro (ed.) *et al.*, J. Phys. G**32**, (2006) 1295.

[16] ALICE Collaboration, K. Aamodt *et al.*, "Production of pions, kaons and protons in pp collision at $\sqrt{s} = 900$ GeV with ALICE at the LHC", to be submitted to Eur. Phys. J. C.

[17] J. Podolanski and R. Armenteros, Phil. Mag. **45**, (1954) 13.

[18] K. Nakamura *et al.* (Particle Data Group), J. Phys. G **37**, 075021 (2010).

[19] W. Blum and L. Rolandi, Particle Detection with Drift Chambers, Springer, Berlin, 1998.

[20] M. G. Albrow *et al.*, Tevatron-for-LHC Conference Report of the QCD Working Group, Fermilab-Conf-06-359, hep-ph/0610012.

[21] R. Brun *et al.*, 1985 "GEANT3 User Guide", CERN Data Handling Division DD/EE/841; R. Brun *et al.*, 1994 "CERN Program Library Long Write- up, W5013, GEANT Detector Description and Simulation Tool".

[22] ALICE Collaboration, K. Aamodt *et al.*, Phys. Rev. Lett. **105**, (2010) 072002.

[23] P. Christakoglou et al., ALICE Internal Note ALICE-INT-2008-010 (2008); P. Christakoglou et al., ALICE Internal Note ALICE-INT-2010-006 (2010); P. Christakoglou et al. [ALICE Collaboration], PoS (EPS-HEP 2009) 405.

[24] G. Bendiscioli and D. Kharzeev, Riv. Nuovo Cim. 17N6, (1994) 1.

[25] STAR Collaboration, B. I. Abelev *et al.*, Phys. Rev. C**75**, (2007) 064901.

[26] A. Moraes (ATLAS Collaboration), ATLAS Note ATL-COM-PHYS-2009-119 (2009).

[27] P. Z. Skands, Contribution to the 1st International Workshop on Multiple Partonic Interactions at the LHC, Perugia, Italy, Oct. 2008, Fermilab-Conf-09-113-T, arXiv:0905.3418[hep-ph] and arXiv:1005.3457[hep-ph].

[28] STAR Collaboration, J. Adams *et al.*, Phys. Rev. Lett. **97**, (2006) 132301.

[29] M. Bourquin and J. M. Gaillard, Nucl. Phys. B**114**, (1976) 334.

[30] UA5 Collaboration, R. E. Ansorge *et al.*, Z. Phys. C**41**, (1988) 179.

[31] CDF Collaboration, F. Abe *et al.*, Phys. Rev. D**40**, (1989) 3791 RC.

[32] UA5 Collaboration, G. J. Alner *et al.*, Phys. Rep. **154** (1987) 247.

[33] UA5 Collaboration, R. E. Ansorge *et al.*, Nucl. Phys. B**328**, (1989) 36.

[34] STAR Collaboration, J. Adams *et al.*, Phys. Lett. B**612** (2005) 181.

[35] STAR Collaboration, B. I. Abelev *et al.*, Phys. Rev. C**79** (2009) 064903.

[36] E735 Collaboration, T. Alexopoulos *et al.*, Z. Phys. C**67** (1995) 411.

[37] CDF Collaboration, D. Acosta *et al.*, Phys. Rev. D**72** (2005) 052001.

[38] UA1 Collaboration, G. Bocquet *et al.*, Phys. Lett. B**366**, (1996) 441.